ISSN 0016-8521, Geotectonics, 2023, Vol. 57, No. 5, pp. 541–570. © Pleiades Publishing, Ltd., 2023.
Russian Text © The Author(s), 2023, published in Geotektonika, 2023, No. 5, pp. 3–36.

Oceanic Crust Formation in the Mid-Atlantic Ridge Segment between Azores and Icelandic Plumes: Results of Geological and Petrogeochemical Studies

S. G. Skolotnev[a], *, A. A. Peyve[a], S. Yu. Sokolov[a], S. A. Dokashenko[a], V. N. Dobrolyubov[a], O. I. Okina[a], B. V. Ermolaev[a], and K. O. Dobrolyubova[a]

[a] *Geological Institute, Russian Academy of Sciences, bld.7, Pyzhevsky per, Moscow, 119017 Russia*

**e-mail: sg_skol@mail.ru*

Received July 6, 2023; revised August 8, 2023; accepted August 22, 2023

Abstract—The structure of the ocean floor and the composition of basalts and dolerites of the MAR segment between the Maxwell and Charlie Gibbs FZs (North Atlantic) were studied based on the data obtained during the 53rd cruise of the R/V *Akademik Nikolaj Strakhov* organized and performed by the Geological Institute of the Russian Academy of Sciences over the period of July 7–August 15, 2022. In this segment, areas of greater and lesser magmatic productivity, which correspond to higher and lower bottom relief, alternate along the spreading axis. In high-relief areas, spreading cells form in the axial zone, and rises of tectonic and volcanic genesis dominate in the crest zone. In low-relief areas, the rift valley consists of deep rift basins; low ridges are developed on the flanks, which are separated by wide depressions. Oceanic N- and T-type tholeiites and E-MORB-type basalts and dolerites are distinguished among the studied volcanics. The N-tholeiites are widespread and were derived from mainly depleted mantle (source of DM). E-MORB-type basalts and dolerites are found in high-relief areas. Their mantle substrate is formed by a mixture of DM and EM-2 material with the subordinate role of HIMU. T-MORB volcanics are mainly localized on large volcanic rises in the southern part of the studied MAR segment and were melted from a substrate formed by a mixture of DM and HIMU material with the subordinate role of EM-2. Two types of mantle inhomogeneities involved in melting are reconstructed: passive and active. The former are represented by blocks of the transformed continental lithosphere that are similar in composition to the EM-2 mantle source. Active inhomogeneities associate with the uplift near Maxwell FZ of the microplume of the enriched mantle with a composition close to HIMU and with its subaxial flow in the north direction up to the Charlie Gibbs FZ.

Keywords: oceanic crust, spreading, rift valley, bottom rise, mantle inhomogeneities, basalt, dolerite, Mid-Atlantic Ridge, North Atlantic

DOI: 10.1134/S0016852123050084

INTRODUCTION

The formation of oceanic crust in spreading zones, the mechanisms of its formation, and the causes of diversity are of undoubted interest to geologists. The variety of mechanisms of oceanic crust formation is determined by the geodynamic spreading regime, the material and temperature heterogeneity of the upper mantle, the influence of lower mantle plumes, and the structure of the ocean floor, which is reflected in the composition, thickness, and structure of the oceanic crust and the nature of the combination of these parameters along the spreading axis.

The geodynamic regime of spreading is determined by the spreading rate and the ratio of tectonic and magmatic processes changing along the spreading axis. The intensity of the influence of deep mantle plumes depends on their composition and size and reaches the peak at the presence of large plumes localized near the spreading axis, which include the Icelandic and Azores plumes located in the North Atlantic [15, 38].

The influence of the axial Icelandic plume on the processes occurring in the spreading zone to the south of it is reflected in the structure and composition of the rocks of the Reykjanes spreading ridge and is associated with the along-axis sublithospheric flow of the plume matter in a southwesterly direction, oriented at an angle relative to the spreading [26, 36] (Fig. 1).

The end of the Reykjanes Ridge near the Bight Fracture Zone (FZ) (57° N) is the southern boundary of the influence of the Icelandic plume since the structures of the Mid-Atlantic Ridge (MAR) extend further south orthogonally to the spreading axis [16]. One can expect that the influence of the Azores plume in the north direction is limited by the Maxwell FZ (47.8° S) where the MAR strike changes from northeast to northwest [44, 47] (see Fig. 1).

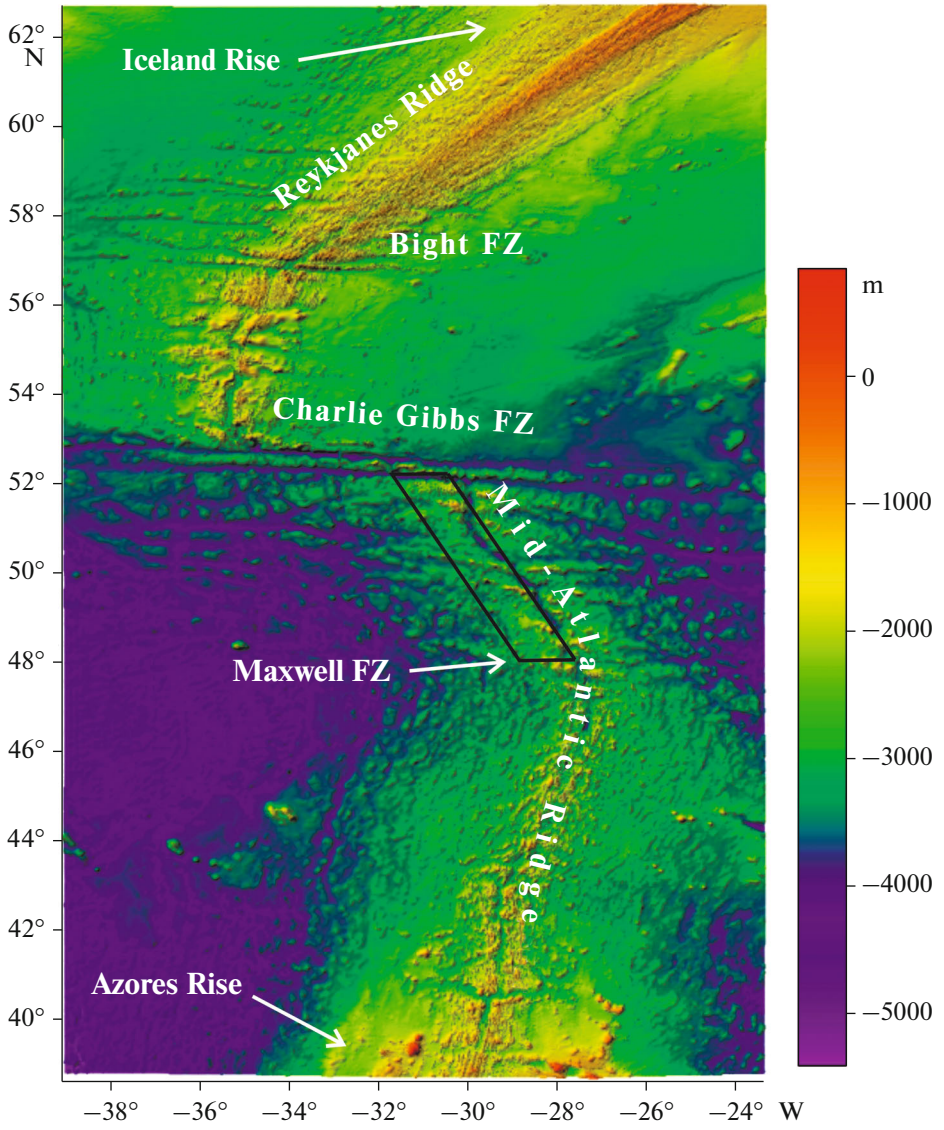

Fig. 1. Structural scheme of the Mid-Atlantic Ridge in the Northern Atlantic (after [21]). The area of works during the 50 and 53 cruises of R/V *Akademic Nikolaj Strakhov* (the depth scale is shown on the right).

During geological and geophysical research in the area of the Charlie Gibbs Fracture Zone (52°–53° N) located between the Bight and Maxwell FZs on the 50th cruise of the R/V *Akademik Nikolaj Strakhov* organized and performed by Geological Institute of Russian Academy of Sciences (Moscow, Russia) over the period of September 8–October 23, 2020, in the North Atlantic, it was found that rift ridges, slightly varying in height and width, reach the fault to the south of the fracture zone [10, 48].

These observations indicate a weakening of the cooling effect of the fracture zone. This effect, as a rule, sharply reduces the intensity of magmatism, consequently, there was an additional source of heating that heated of the sublithospheric mantle south of the Charlie Gibbs FZ and suggests that the hotter substance of the sublithospheric along-axis flow from the Azores plume was a source of additional heat [33].

However, the character of variations in the axial depth and composition of basalts along the MAR axis in the North Atlantic does not allow us to draw such an unambiguous conclusion. Except for several sharp rises, the depth of the rift valley from the Azores Rise to the Maxwell FZ gradually increases from 2000 to 3000 m on average [21] (Fig. 2a).

North of the 49° N, the rift valley depth increases sharply to 3700 m on average and remains unchanged to 51.5° N. It decreases again near the Charlie Gibbs FZ. The rift valley depth from the Iceland Rise to the Bight FZ gradually increases from 200 to 2700 m on average.

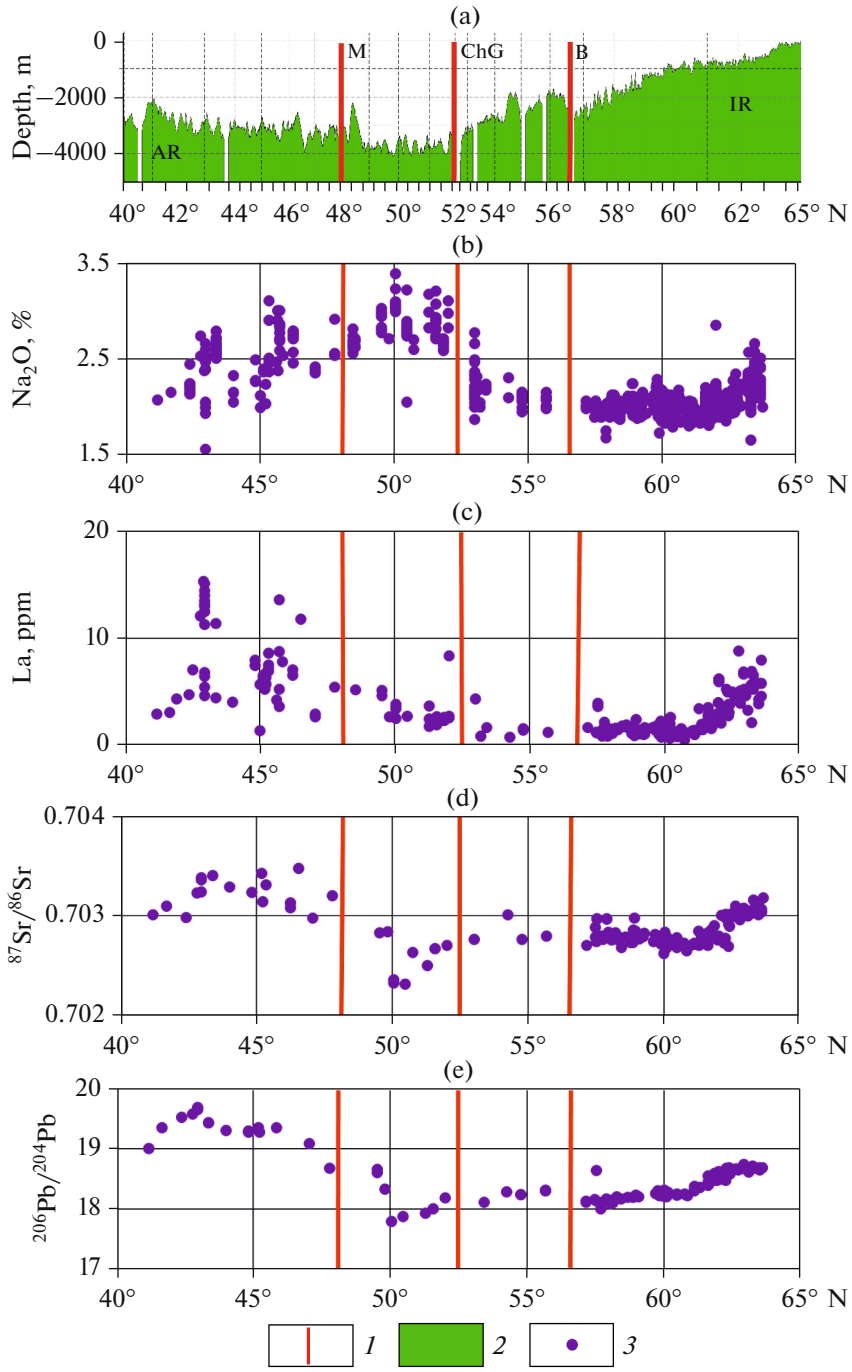

Fig. 2. Variations in the depth of the MAR axis, contents of Na_2O (%), La (ppm), and $^{87}Sr/^{86}Sr$ and $^{206}Pb/^{204}Pb$ isotope ratios in basalts of the Mid-Atlantic Ridge (MAR) between the Azores Rise and Iceland Rise (according to [21, 44, 56]). Rises: AR, Azores; IR, Iceland. Fracture zones: B, Bight; ChG, Charlie Gibbs; M, Maxwell. (*1*) The position of the fracture zones; (*2*) the profile of the MAR axial topography; (*3*) composition points.

One can observe a rise of the valley bottom to an average depth of 2100 m between the Bight FZ and 54.3° N, and then a sharp subsidence of the ocean floor to a depth of 2700 m. From the 54.3° N to the northern branch of the Charlie Gibbs FZ, the valley bottom depth gradually increases to 3000 m.

The most subsided section of the MAR rift valley between the Azores and the Iceland is in the segment of 49°–51.5° N. In general, the more greater the depth of the rift valley, the less intense the magmatic accretion of the crust, the lower the temperature of the upper mantle and the lower the degree of its partial

Table 1. Isotope compositions of collected samples of basalts and dolerites

Ser. no.	Sample	$^{87}Sr/^{86}Sr$	$^{143}Nd/^{144}Nd$	$^{206}Pb/^{204}Pb$	$^{207}Pb/^{204}Pb$	$^{208}Pb/^{204}Pb$
1	S5322/1	0.703402	0.513083	19.07	15.59	38.47
2	S5324/7	0.703711	0.512981	18.49	15.53	38.48
3	S5329/7	0.703598	0.513006	18.59	15.49	38.33
4	S5330/3	0.702917	0.513164	18.28	15.58	38.60

melting [32]. The decrease in the degree of the upper mantle melting is confirmed by high Na_2O content in the basalts of this MAR segment (see Fig. 2b).

The MAR segment (49°–51.5° N) is an area of the coldest upper mantle and it is quite likely that it is not affected by plumes. In addition to temperature, the higher contents of lithophilic elements and a number of radiogenic isotopes in the composition of basalts serve as indicators of the influence of plumes. There is a counter decrease in the contents of La and other lithophilic elements and $^{87}Sr/^{86}Sr$ and $^{206}Pb/^{204}Pb$ ratios in basalts north of the Azores and south of the Icelandic plumes to the 50th parallel north, which may be the boundary between the regions of influence of the Icelandic and Azores plumes [44, 47] (Figs. 2c–2e).

The geological boundary between the regions of influence of the Icelandic and Azores plumes depends on the choice of parameters. Since this caused the need for additional research, a detailed study of the processes of crustal accretion and structure formation in the MAR segment between the Maxwell and Charlie Gibbs FZs was carried out during the 53rd cruise of the R/V *Akademik Nikolaj Strakhov* [4, 5].

The present paper aims at analyzing the results of studying the composition and structural confinement of volcanic rocks dredged during the 53rd cruise of the R/V *Akademik Nikolaj Strakhov* in 2022.

MATERIALS AND METHODS

During field studies, a bathymetric survey of the ocean floor was carried out using a SeaBat 7150 deep multibeam echosounder (RESON company). The survey covers the axial and crest zones of the Mid-Atlantic Ridge (MAR) in the segment between 48° N and 51° N (hereinafter, the Faraday polygon area). The bathymetric map constructed on the basis of the survey data served as the basis for the selection of sampling sites [4] (Fig. 3).

A collection of rocks (basalts, gabbroids, ultramafic rocks, dolerites, metasomatic rocks, limestones, and breccias) was collected at 32 dredging stations. The coordinates of the sampling points are given in [4] (see Fig. 3). We have studied dolerites and basalts.

The bulk composition of rocks was studied by X-ray fluorescence analysis (XFA) on an S4 Pioneer X-Ray spectrometer (Bruker, Germany) in the Chemical Analytical Laboratory of the Geological Institute (Russian Academy of Sciences, Moscow, Russia). Sr, Zr, V, Cr, and Ni contents in some samples were measured with the XFA method also. The measurement results are represented in Supplement 1 (Table S1).

After analyzing the bulk compositions, key samples were selected for geochemical studies. The contents of trace elements were measured by inductively coupled plasma mass spectrometry (ISP-MS) in the Chemical Analytical Laboratory of Geological Institute of Russian Academy of Sciences (Moscow, Russia) on the Element-2 mass spectrometer (Thermo Fisher Scientific, Germany). The method used to determine trace elements in rocks is described in [40, 41]. The measurement results are represented in Supplement 2 (Table S2).

After processing the geochemical data, the $^{87}Sr/^{86}Sr$, $^{143}Nd/^{144}Nd$, $^{206}Pb/^{204}Pb$, $^{207}Pb/^{204}Pb$, and $^{208}Pb/^{204}Pb$ isotope ratios were studied in the most representative samples at the Isotope Research Center of All-Russian Scientific Research Geological Institute (VSEGEI) (St. Petersburg, Russia). The measurement methodology is described in [12]; the measurement results are presented in Table 1.

Along with the rocks of the Faraday polygon area, we have studied the basalts dredged during the 50th cruise of the R/V *Akademik Nikolaj Strakhov* (September 8–October 15, 2020) in the MAR segment between the Faraday polygon area and the Charlie Gibbs FZ.

STRUCTURAL ZONATION OF THE FARADAY POLYGON AREA

The Faraday polygon area is located north of the Maxwell FZ, where the general strike of the Mid-Atlantic Ridge (MAR) changes from northeast ∟ ~ 20° to northwest ∟ ~ 337°. In this area, the direction of spreading is submeridional at an angle of ∟96° [5, 37] (see Fig. 1).

The Faraday polygon covers the axial and crest zones of the MAR between the 48° N and 51.3° N; several segments of different structure are replaced along the strike of the MAR (see Fig. 3).

Structure of the Segments of the Faraday Polygon Area

Segment 1. This segment extends from the northern boundary of the polygon to the latitude of 50.70° S. At

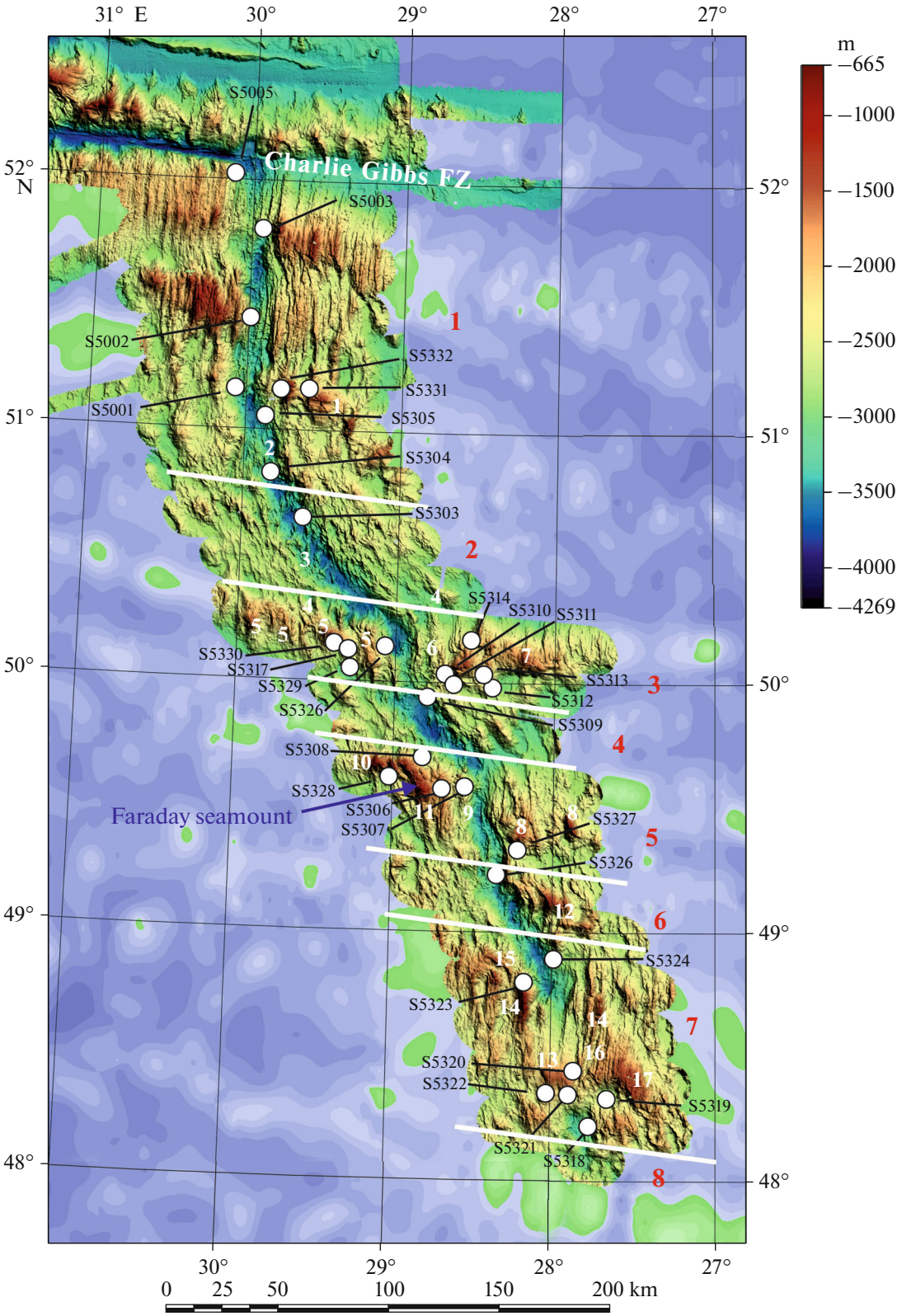

Fig. 3. Bathymetric map and scheme of sampling the axial and crest zones of the Mid-Atlantic Ridge between the Charlie Gibbs and Maxwell FZs (according to the data of the 50th and 53rd cruises of R/V *Akademik Nikolaj Strakhov* [4, 10, 48]). Figure shows boundaries (lines in white) between segments of different structures; numbers of segments (numbers in red); sites of successful dredging (circles in white), numbers of sites; depth scale (top right). The numbers of morphostructures are indicated (numbers in white) according to the order of mention in the text: oceanic core complexes (*1*, *8*, *12*, *15*); rift basin (*2*); neovolcanic ridge (*3*); nontransform displacement (*4*); rift mountains (*5*, *6*, *9*, *16*); Rise: oval (*7*), volcanic (*10*, *17*), neovolcanic (*13*); Faraday seamount (*11*); depression (*14*).

this site, the rift valley extends orthogonally to the direction of spreading at an angle of 6°.

Segment 1 consists of two spreading cells that continue each other with almost no displacement [1, 23, 35]. The rift valley 15–17 km wide in the central parts of the cells has the lowest depth up to 3240 m, which increases to both distal parts by 500–550 m. Neovolcanic ridges up to 10 km long, up to 1.5 km wide, and up to 100 m high have formed in the central part of the cells. Fresh pillow basalts were dredged at the S5305 station on the slopes of the neovolcanic ridge of the more southern cell.

Rift mountains, mostly oriented parallel to the rift valley, are common in the crestal zone of the MAR opposite these cells. In the more northern cell, these ridges are up to 6 km wide and up to 700 m high; small low ridges are in the more southern cell (3 km wide and 400 m high). On the eastern flank of the more northern cell within the Faraday polygon area are two dome-shaped rises approximately 13 × 10 km in size, rising to a depth of 1030 m (see Fig. 3, *1*).

Tectonic corrugations are visible on their surface. This is evidence that they are oceanic core complexes (OCC), i.e., structures characteristic of distal parts of spreading cells with reduced magmatism [19]. This is confirmed by the data on their sampling; basalts, gabbroids, and serpentinized peridotites were dredged at their slopes (stations S5331 and S5332).

Between Site 1 and the Charlie Gibbs FZ are three typical spreading cells, slightly displaced relative to each other by nontransform offsets. Rift valleys are orthogonal to the spreading axis here and are composed of basalts. The bottom of the rift valley in the central part of the northernmost cell reaches shallow depths of 2750 m. The rift ridges located opposite this cell join the valley of the Charlie Gibbs FZ without changing in width and height.

Basalts have been dredged from the rift-fault intersection zone, where deep rocks are common (station S5005). These facts indicate a high intensity of magmatic activity within this spreading cell, which is slightly reduced by the cooling effect of the large Charlie Gibbs transform fault.

Segment 2. This segment located southward from Segment 1 and stretches to the latitude of 50.25° N. The rift valley as a whole has a 320° strike oblique to the spreading axis; there are no spreading cells. The axial zone consists of several deep isometric rift basins with an average diameter of 8 km and a bottom depth of up to 4250 m (see Fig. 3, *2*).

Each more northern basin is shifted to the west by 3–5 km relative to the more southern basin. The basins are separated by small rises reaching a depth of 3970 m, which are terminated by narrow low neovolcanic ridges 3–8 km long, up to 2.5 km wide, and 100–250 m high, mostly orthogonal to the direction of spreading (see Fig. 3, *3*). Pillow basalts were dredged at the slopes of two such rises (stations S5303 and S5304). In the crestal zone are low ridges, oriented mainly parallel to the rift valley.

Segment 3. This segment, extending to the parallel 49.90° N, is separated from Site 2 by a nontransform displacement with an offset of ~18 km. It extends along the latitude 50.25° N and represents a depression up to 4100 m deep (see Fig. 3, *4*).

The axial zone of Segment 3 is a spreading cell, in the central part of which the rift valley bottom of a submeridional strike is located at noticeably lower depths, 3500 m, than in its distal parts, 3750 m.

A narrow (up to 1 km) neovolcanic ridge with a height of 250 m stretches in the central part.

Serpentinized ultramafic rocks, gabbro, and dolerites were dredged at station S5316 on the western side of the rift valley, in its northern distal part. Both flanks of the ridge zone are linear uplifts elongated parallel to the direction of spreading. Their average depth is approximately 2100 m, and the minimum depths reach up to 1430 m (in the west) and 1270 m (in the east). The structure of the flanks is asymmetrical.

On the western flank is a system of subparallel ridges with a strike of ∟340°, obliquely located relative to the direction of spreading (Fig. 3, *5*). Some ridges are crowned with volcanic edifices. Their length (20–25 km) is proportional to that of the spreading cell, the width varies from 2 to 4 km, and the average height of the separating depressions above the bottom is 500–750 m.

Mainly basalts and subordinate dolerites, gabbroids, and ultramafic rocks were dredged from the slopes of one of these ridges at stations S5317, S5329, and S5330. Furthermore, secondary minerals in basalts from the deepest station S5329 are represented by chlorite, by smectite at the intermediate station S5317, and basalts are fresh at the shallowest station S5330. This fact indicates that a relatively thick basalt section has been sampled on this ridge, since, in accordance with the distribution of clay minerals along the basalt section in the rift valley, chlorite is replaced by smectite at a depth of approximately 500 m [14].

Along the eastern flank for a distance of ~20 km, directly near the rift, there are several subparallel ridges with a strike orthogonal to the direction of spreading, with summits at an average depth of 2700 m (see Fig. 3, *6*).

Further to the east there occurs a series of jointed oval rises with an average diameter of approximately 16 km and a height of 2000 m above the bottom (see Fig. 3, *7*).

Mainly serpentinized ultramafic rocks, a small number of gabbroids, basalts, and dolerites were dredged from the slopes of oval rises at stations S5310, S5311, S5312, S5313, and S5314.

Segment 4. This segment with structures oblique to the spreading axis extends to the 49.65° N. The strike of the rift valley and rift mountains is ∟330°. In terms

of the structure, this site is similar to that of Segment 2. Echeloned rift basin are up to 4250 m deep. The rift mountains are larger than these structures in Segment 2; their width is 4–5 km on average and summits reach depths of 2500 m. At station S5309, basalts are dredged from the eastern side of the rift valley.

Segment 5. The next Segment 5 with structures orthogonal to the spreading axis extends to the 49.15° N and is separated from Segment 4 by a nontransform offset of 6 km. The site consists of two spreading cells separated by a small nontransform offset of ~2 km.

In the northern cell, the rift valley floor rises to a depth of 3250 m in the central part, while it descends in the distal parts to a depth of 4000 m in the south and to a depth of 3900 m in the north.

Small neovolcanic ridges were formed in the least deep parts of the rift valley. Basalts and some dolerite and gabbro were dredged from the sides of the rift valley at stations S5307 and S5326.

On the eastern flank opposite the northern cell, one can observe the typical rift mountains with well-developed ridges parallel to the rift valley. Some of the latter join dome-shaped rises in the south, which are similar to the OCC in their structural position and size (approximately 10 × 10 km in plan, summits up to 2000 m) (see Fig. 3, *8*).

This is also evidenced by the sampling data of one of these ridges, as mainly serpentinized ultrabasites were dredged from its slope at station S5327.

On the western flank are two ridges parallel to the rift valley in the near-rift zone (see Fig. 3, *9*).

Further to the west, there is an uplift of closely adjacent ridges and oval uplifts (see Fig. 3, *10*).

The average depth level of the uplift is approximately 2000 m, and the lowest depth (less than 1000 m) is observed at Faraday Seamount [21] (see Fig. 3, *11*).

The ridges within the uplift have a strike from 330° up to 340°. Gabbro, fresh basalts with smectite, and dolerites were dredged from two different slopes of Faraday Seamount (stations S5306, S5308); only basalts with smectite were dredged from the westernmost seamount of the uplift (station S5328).

On the flanks of the southern spreading cell, the relief is lower; only the near-rift ridges on both flanks are higher and more extended; further on the flanks, the shallow ridge relief with dominance of depressions prevails. The strike of the structures is oblique relative to the spreading.

Segment 6. The more southerly Segment 6 with structures oblique relative to the spreading extends to the 48.85° N, and the rift valley strike is 345°. In the axial part, it is structurally similar to other sites, where the rift valley is oblique (Segments 2, 4), but there are noticeable differences in the crestal zone.

The western flank has a low, shallow ridge topography similar to that in the southern part of the more northerly Segments 5. The eastern flank is essentially higher and consists of high ridges with a strike of 345°, enclosing several dome-shaped rises ranging in size from 5 × 5 km to 10 × 10 km, reaching depths of 1900 m (see Fig. 3, *12*).

Serpentinized peridotites and a small amount of basalts were dredged from the slopes of one of these ridges at station S5324.

Segment 7. The next southward Segment 7 with structures orthogonal to the spreading axis extends to 48.25° N. Recently, this site represents a single extended spreading cell.

The rapid rise of the rift valley bottom begins from a depth of 3500 to 3000 m on both distal parts of the cell; in the center of the cell, shifted to its southern part, the rift valley disappears since a large oval rise of ~20 km across formed here reaching a depth of 1600 m; its height above the rift valley floor is 1400 m (see Fig. 3, *13*).

It is of volcanic origin since fresh basalts were dredged from its slope (station S5322). Two neovolcanic ridges, 2–4 km wide and up to 1000 m high, branch off from this neovolcanic rise in a northerly direction. The structure of the crestal zone shows that two spreading cells existed earlier at Segment 7. Furthermore, systems of typical rift mountains, separated on each flank by depressions, formed opposite each of them on both flanks (see Fig. 3, *14*).

In the northern cell, some ridges of rift mountains on the western flank join oval and oblong rises of 10 × 12 km in size on average, merging with each other and rising to an average depth of 1300 m (see Fig. 3, *15*).

Only gabbroids were dredged from the slope of one of the ridges (station S5323). On the eastern flank of the crestal zone, opposite to the southern spreading cell are narrow (2–3 km), high (summits at depths up to 1700 m) extended, closely spaced ridges. Basalts were dredged from the latter (stations S5320 and S5321) (see Fig. 3, *16*).

This system of ridges ends in the east with a large elongated high rise of 20 × 30 km in area, rising to a depth of 1400 m. It is terminated by shallow ridges with a strike close to that of the rift valley (see Figs. 3, *17*). We assume that this rise is also of volcanic origin since basalts and dolerites were dredged from its slope (station S5319).

In relatively recent times, within Segment 7, the southern spreading cell was prograded into the area of the northern cell. Given that a large neovolcanic rise formed at that time in the axial zone of the southern cell, one can expect that the cause of this progradation is a dramatic increase in magmatic activity in the southern cell.

Segments 8. This is the last site to the south, extending to the end of the Faraday polygon area. It appears to be represented only by its northern fragment, enclosing a rift basin with a small neovolcanic ridge extending orthogonally to the spreading axis. On

both flanks is a symmetrically developed system of rift mountains formed by ridges of moderate height with a strike of 330° oblique to the spreading axis.

Structural Features of the Faraday Polygon Area

Two main structural features were identified in the Faraday polygon area.

Throughout the Faraday polygon area, the areas with low and high relief of the floor along the MAR axis alternate. In the high-relief segments (1, 3, 5), the rift valley depth ranges from 3240 to 4000 m, while it varies from 3970 to 4250 m in the low-relief sites (2, 4, 6) (see Fig. 3).

At Segment 7 with the highest relief, the rift valley depth varies between 3000–3500 m. The structure of the axial zone of the high-relief areas, except for Site 7, is characteristic of typical spreading cells. The rift valley is the deepest in the distal parts and its bottom rises toward the central part. The latter is the center of subaxial upwelling of the asthenospheric mantle (diapirism) and, accordingly, of magmatic activity weakening towards the distal parts of the cell [1, 17, 33, 42].

The largest neovolcanic ridges are in the central parts of the cell. The crestal zones at these segments also have elevated relief and have different structures at different sites. Furthermore, the western and eastern slopes of the cell are asymmetric in each case.

In the northernmost Segment 1, the structure of the crestal zone is the most typical of such zones. Rift mountains similar in structure are formed on both flanks. However, several dome-shaped OCCs formed in the distal part of the southern cell on the eastern flank.

At Segment 3, a system of large high ridges of northwestern strike, separated by broad and deep depressions and composed of basalts, is developed on the western flank. The structure of the eastern flank of this site is dominated by a system of oval rises similar to those formed by the oceanic core complexes (OCCs). Despite the fact that they are also composed of deep rocks, they cannot be attributed to OCCs because the shallow structures superimposed on their surface are orthogonal to the spreading axis. Given the wide distribution of serpentinized ultramafic rocks within the shallow structures, it can be expected that they were formed as a result of uplift of lithosphere blocks caused by processes of serpentinization of the upper mantle.

We observed a similar structural paragenesis in the area of the Doldrums megatransform system, where systems of large ridges (former neovolcanic ridges) were formed on the western flank between the Vernadsky–Pushcharovsky–Bogdanov fracture zones, while systems of oval rises composed of serpentinized ultramafic rocks were formed on the eastern flank [9].

It was suggested that such a structural paragenesis is formed under the deficient magmatic budget. Furthermore, rare but strong pulses of magmatism occur, leading to the formation of large neovolcanic ridges. In the intervals between magmatic pulses, serpentinization of closely adjacent mantle material occurs within the rift valley floor with subsequent uplift of its individual blocks and formation of oval rises. We assume that a similar mechanism of formation of ridge structures can be applied to Segment 3 of the Faraday polygon area.

On the eastern flank of Segment 5, typical rift mountains and domed-shaped OCC structures are developed. The western flank of Segment 5 is one of the elevated fragments of the whole Faraday polygon area, where a system of high oblique ridges of northwestern strike and adjacent oval and elongated rises, which are similar in size and morphological properties to the large neovolcanic uplift at Segment 7, was formed. One of the rises is composed of basalts, which suggests the volcanic nature of this system of ridges and uplifts (block). Along with basalts and dolerites, gabbroids were dredged from the foot of the seamount Faraday.

Based on the analysis of the obtained data, we believe that the western flank of Segment 5 was formed in the axial spreading zone under conditions similar to those that exist at present in the axial part of Segment 7 but in an earlier epoch. In accordance with the age of the ocean floor determined by identification of the linear magnetic anomalies [4, 5], this occurred ~2.58 Ma ago, when magmatic activity was apparently much more intense in this area. It is obvious that this section of the ocean floor has experienced block uplift since its formation, resulting in the exposition of deeper rocks, gabbroids.

Segment 7 is characterized by the anomalous structure of the axial zone due to the formation of a large volcanic rise here that blocked the rift valley and made it unusually elevated in the distal parts of the cell. To date, this is evidence that this area is the center of the most intense magmatism. There were also bursts of intensity in earlier epochs, which is correlated with the formation of a large volcanic rise on the eastern flank of the ocean floor section with an age of 2.58 Ma [4, 5]. The center of the most intense magmatic activity in the studied MAR segment probably shifted ~2.58 Ma ago from Segment 5, where Faraday Seamount was formed, to the Segment 7 area.

The low-relief areas have a different structure. Here, the rift valley consists of separate deep rift basins, the more northerly echelon-like basins are displaced to the west relative to the more southern basins. The basins are separated by shallow neovolcanic ridges orthogonal to the spreading axis.

At these segments, low relief formed on the flanks of the MAR, which was formed by ridges and small low ridges of northwestern strike separated by broad depressions. Sometimes, OCC-type dome-shaped rises are observed here. According to all indications, the low-relief sites are the areas of the lowest magmatic activity and productivity, both now and in the past. In the southernmost Segment 6, the height of ridges on the flanks is much higher than at Segments 2

and 4, which indicates that volcanic activity is more intense here than at the lower-relief sites.

The peculiarities of the distribution of the intensity of magmatism and crustal accretion over the Faraday polygon area are confirmed by the character of the distribution of Bouguer gravity anomalies (AB) [5]. The most extensive area of their lowest values, corresponding to the greatest crustal thickness and/or greater heating of the sublithospheric mantle, is observed in the area of Segment 7, where the axial volcanic rise and high volcanic rises on the eastern flank were formed.

The fields of the lowest values are also isolated in other high-relief sites: 1, 3, and 5. Furthermore, Segment 1 also passes into a very extensive area of low AB values located directly to the south from the Charlie Gibbs FZ [5]. The axial zone of all low-relief sites is dominated by fields of significantly higher Bouguer anomalies, extending in the northwestern direction.

Thus, it can be stated that the Faraday polygon area represents alternation of areas with higher and lower intensity of magmatic productivity of the crust and, respectively, with higher and lower temperature of the upper mantle:

— the former are high-relief areas,

— the latter are low-relief areas.

Furthermore, the average elevation of both low-relief and high-relief areas decreases from Segment 7 in the northern direction and increases again directly in the Charlie Gibbs FZ area.

The next structural feature of the Faraday Polygon area is the overlap of two structural patterns:

— submeridional, orthogonal to the spreading axis;

— northwestern, oblique to the spreading axis.

The submeridional structures dominate in high-relief areas. The NW-striking structures dominate in low-relief areas, although there are also submeridional structures manifested in the form of small neovolcanic ridges formed within rift-related depressions.

PETROGEOCHEMICAL AND ISOTOPE CHARACTERISTICS OF BASALTS AND DOLERITES

Petrography

Aphyric basalts predominate in the collection. In thin sections of well-crystallized rock varieties, one can observe that there occurs irregularly shaped clinopyroxene grains and subordinate amounts of opaque grains of ore mineral in interstitial space between plagioclase microliths.

In most basalts, rhomboid olivine subphenocrysts (0.25–0.5 mm in size, 1–3 vol %) are common, and they sometimes occur as intergrowths with plagioclase and clinopyroxene subphenocrysts (up to 1 mm in size).

Plagioclase porphyritic basalts are dominated by plagioclase porphyritic varieties. Based on the amount of phenocrysts, they are subdivided into sparsely (1–2 vol %), moderately (3–4 vol %), and abundant (6–10 vol %) porphyritic.

The phenocrysts are represented by tabular phenocrysts (1–12 mm) and xenocrysts irregular in shape (3–15 mm), often in the form of aggregates of several grains. Some xenocrysts contain rod-shaped apatite inclusions. Among rarely occurring minerals are:

— olivine (1–3 vol %);

— plagioclase, clinopyroxene (1–3 vol %);

— plagioclase and olivine (1–2 vol %)

— porphyritic basalts.

Clinopyroxene and olivine phenocrysts are 0.8–1.5 mm in size.

Among the basalts are varieties with a large amount of ore mineral (2–3 vol %), while it is not more than 1 vol % in the overwhelming number of samples. Basalts are slightly to moderately porous (1–5 vol %). Rounded vesicles of 0.15–3 mm in diameter are more often empty.

Basalts dredged from the rift valley are fresh. Beyond the rift valley, secondary minerals (from 2–3 to 10 vol %) develop in basalts. Smectite predominates, chlorite is less common, and partial palagonitization of quenching glass is observed.

Dolerites are sharply different from basalts in their texture. They are characterized by close size and degree of idiomorphism of plagioclase and clinopyroxene grains. Aphyric and plagioclase (2–6 vol %) porphyritic varieties are distinguished among them. There are samples with a large number of ore minerals (2–3 vol %). Dolerites are altered, from 2–3 vol % to 8–10 vol %.

Chlorite, sometimes together with actinolite, partly develops after all rock-forming minerals; plagioclases are partly albitized, ore mineral may be replaced by leucoxene.

Variations in the Bulk Composition of Rocks

The studied basalts and dolerites are characterized by a great variety of compositions, the regularities of variations allow one to reveal the analysis of double variation diagrams.

Based on MgO-oxide variation diagrams constructed on the data from Supplement 1: Table S1, several groups (types) of basalts and dolerites united by common petrochemical parameters were distinguished. To describe these groups, we also used data on Cr, Ni, V, Zr, and Sr contents determined by the X-ray fluorescence method (Fig. 4).

Several of these groups (hereafter referred to as coherent groups) form extended subparallel fields in one or more diagrams (see Fig. 4). The coherent groups also include the main group, which unites most studied volcanics with moderate contents of oxides and elements under consideration.

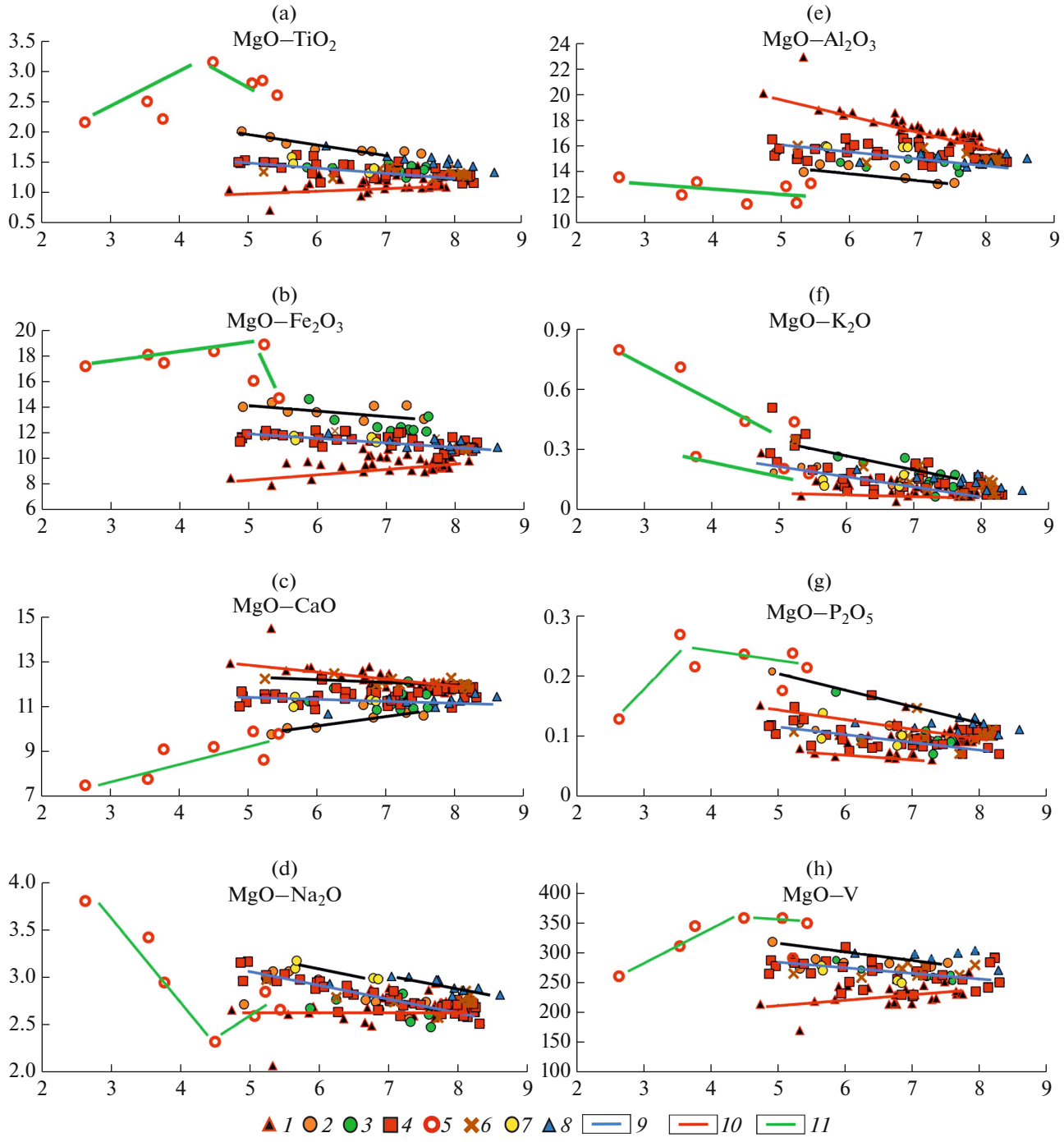

Fig. 4. Diagrams of variations in contents of rock-forming oxides (%) and V (ppm) depending on the MgO content (%) in basalts and dolerites. The trends of variations (lines in black) in the composition of rocks within the groups: (a) high-Ti, high-Fe, and high-Ti; (b) high-Fe and high-Ti high-Fe; (c) high-Ca (upper line) and high-Ti high-Fe (lower line); (d) high-Na and high-Ti; (e) high-Ti, high-Fe; (f) high-K; (g) high-P; (h) high-Ti. (*1*–*8*) Petrochemical groups of basalts and dolerites: (*1*) high-Al, (*2*) high-Ti, high-Fe, (*3*) high-Fe, (*4*) main, (*5*) low-Al, (*6*) high-Ca, (*7*) high-Na, (*8*) high-Ti; (*9*–*11*) trends of compositional variations in petrochemical groups: (*9*) main, (*10*) high-Al, (*11*) low-Al.

The composition points of rocks of the main group on the $MgO–TiO_2$, Fe_2O_3, Na_2O, Cr, Ni, V, Zr, and Sr diagrams form compact fields with distinct trends of increasing (TiO_2, 1.17–1.61%; Fe_2O_3, 10.93–12.14%; Na_2O, 2.52–3.17%; V, 236–310 ppm; Zr, 80–100 ppm; Sr, 100–120 ppm) and decreasing (Cr, 748–134 ppm and Ni, 191–83 ppm) contents with decreasing MgO content (8.3–4.9%).

The field of composition points in the $MgO–Al_2O_3$ diagram (14.66–16.48%) reveals a weak tendency to increase in Al_2O_3 content, while that in the MgO–CaO diagram (10.85–11.65%) is to a decrease in CaO content with decreasing MgO content.

The wide fields of composition points of basalts of the main group are in the $MgO–SiO_2$ (48.64–50.66%), K_2O, and P_2O_5 diagrams.

Such a pattern of variations reflects the process of fractional crystallization of primary basaltic melts, from which more magnesian olivines and clinopyroxenes crystallize during their ascent. The crystallization of these minerals leads to the depletion of the residual melt in Ca, Cr, and Ni and the enrichment in Fe, Ti, Na, V, Zr, Sr, and slightly Al.

In the $MgO–TiO_2$ diagram, a field of volcanics extends subparallel to the field of main rocks. At the same MgO contents, these volcanics are characterized by higher TiO_2 contents compared to the rocks of the main group. Petrographically, they are distinguished by a higher content of Fe-Ti ore minerals (see Fig. 4a).

The field unites two groups of samples. The rocks of one group (samples S5307/1,2,4,5, S5309/7, S5314/1, S5326/4, S5329/5) are also characterized by noticeably higher of Fe_2O_3 and Zr contents and lower Al_2O_3 (13.03–14.55%) and CaO (hereinafter, group of high-Ti high-Fe rocks) contents. Furthermore, TiO_2 (1.66–2.03%), Fe_2O_3 (12.94–14.37%), and Zr (90–138 ppm) contents clearly increase and the CaO content (11.58–9.77%) decreases with decreasing MgO content. Moderately plagioclase porphyritic basalt (sample S5314/1) from this group has higher Al_2O_3 content (15.45%). The Fe_2O_3 content in samples of the second group is the same as in the volcanics of the main group.

However, they are characterized by higher Na_2O (2.82–3.01%) and V (271–303 ppm) contents at TiO_2 (1.35–1.79%) (hereinafter referred to as the group of high-Ti rocks). They are represented by samples S5309/1, S5005/3, 4, 5, 6, 9, 10, 11, 12, and 14 (see Fig. 4).

In the $MgO–Fe_2O_3$ diagram, the field of basalts is subparallel to that of the main group. At the same MgO values, basalts have noticeably higher Fe_2O_3 contents (12.08–14.62%) compared to the rocks of the main group (see Fig. 4b).

This field includes composition points of samples of the high-Ti high-Fe group as well as a large volume of basalts with the same TiO_2 contents as the rocks of the main group (hereafter, the group of high-Fe rocks).

High-Fe basalts (S5304/5, S5309/4,6, S5322/4, S5324/3,5, S5329/6, S5330/5, S5332/2,5) have lower Na_2O (2.48–2.77%) and Al_2O_3 (13.88–15.13%) contents in comparison with the rocks of the main group; some basalts are characterized by very high Cr content (603–976 ppm).

In contrast to the rocks of the main group, the large group of volcanics (S5304/7, S5321/3, S5322/1, S5330/3, S5003/2, 6, 9, 12, 15, 18, 19, 21, 26, 29) is characterized by higher CaO content (11.79–12.47%) (hereinafter, the group of high-Ca rocks) and lower TiO_2 content (1.24–1.44%). The composition points of volcanics are well distinguished in the MgO–CaO diagram (see Fig. 4c).

The field of composition points with lower CaO contents is also clearly distinguished in this diagram. It is formed by volcanics of high-Ti high-Fe, high-Ti, and high-Fe groups.

The field of basalts with higher Na_2O contents is distinguished in the $MgO–Na_2O$ diagram (see Fig. 4d).

A significant part of the field is represented by high-Ti basalts characterized above. However, there are also samples with Na_2O content of 2.99–3.18% but with low TiO_2 contents (S5303/1, S5305/14,15, S5332/6) here (hereafter referred to as the group of high-Na rocks).

Two groups of volcanics that differ markedly in composition from the coherent group rocks are distinguished in the variation diagrams. The more abundant group of them is distinguished on the $MgO–Al_2O_3$ diagram by higher Al content (Al_2O_3 = 16.04–22.92%); that in the MgO–CaO diagram by higher CaO content (11.49–14.48%) at the same MgO contents (hereafter, the group of high-Al rocks) (see Fig. 4e).

These rocks are characterized by lower SiO_2, TiO_2, Fe_2O_3, Na_2O, P_2O_5 V, and Zr contents and higher Sr, Cr, and Ni contents. Two petrographic subgroups are distinguished among high Al volcanics:

1. aphyric (S5303/2,4,5, 7, S5322/5,8);

2. abundant plagioclase porphyritic (S5316/22, S5318/4, S5319/1, S5320/7, S5321/1, S5326/2,7,8, S5330/4, S5001/1-38, S5002/1-7, S5003/1,25,28, S5005/8,13).

Despite such difference in the mineralogical composition, high-Al volcanics in most diagrams form single isolated fields of composition points.

The field of these rocks in the $MgO–Al_2O_3$ diagram shows a distinct trend of increasing Al_2O_3 content with decreasing MgO. In other MgO–oxide diagrams, the TiO_2, Fe_2O_3, Cr, Ni, V, and Zr contents consistently decrease and CaO and Sr contents increase with decreasing MgO (see Fig. 4e).

Such a behavior of elements in plagioclase porphyritic volcanics reflects the sequential increase in the proportion of plagioclase xenokrist in the rock. Obviously, in the case of aphyric rocks, it is possible to expect that plagioclase phenocrysts were successively dissolved in the melt during their formation.

Basalts and dolerites of another independent group, including samples S5324/7, S5328/4, S5329/2,7,9, S5331/1, and S5332/1, differ sharply from the other volcanics by significantly lower Al contents (Al_2O_3 =

11.43–13.54%) (hereafter referred to as the group of low-Al rocks) (see Fig. 4e).

Petrographically, they include aphyric and, rarely, plagioclase porphyritic basalts and dolerite (sample S5329/7), all with large amounts of ore mineral. There are two types of basalt: fresh and altered with either smectite or chlorite.

They are characterized by significantly higher contents of the following components compared to the bulk of the rocks studied:

— TiO_2 (2.17–3.16%);

— Fe_2O_3 (14.70–18.90%);

— P_2O_5, Zr, Sr, V (261–358 ppm)

and lower values of:

— MgO (2.63–5.44%);

— CaO (7.49–9.88%);

— Cr (41–271 ppm);

— Ni (23–101 ppm).

A different distribution pattern of basalts and dolerites by groups is observed on MgO–K_2O, P_2O_5 diagrams. In the MgO–K_2O diagram, composition points of most samples form a compact field with a distinct tendency of increasing K_2O content (from 0.08 to 0.29%) with decreasing MgO content (see Fig. 4f).

A small number of samples (S5318/11, S5319/1,4, S5314/1, S5320/1,2,4,5, S5321/3, S5322/1,5, S5324/3, S5330/3, S5332/2) have higher K_2O content (0.15–0.51%) at the same MgO values (hereinafter, high-K rocks). In general, they are also characterized by higher Sr (125–200 ppm) and P_2O_5 (0.10–0.17%) contents. Among the high-K samples are representatives of several coherent groups distinguished above as well as high-Al volcanics.

Low-Al rocks are also subdivided into low-K (K_2O = 0.18–0.27%) (S5329/2, S5331/1, and S5332/1) and high-K (K_2O = 0.44–0.79%) (S5324/7, S5328/4, S5329/7, S5329/9) (Fig. 4f).

The high-K volcanics have higher P_2O_5 (0.13–0.27% vs. 0.17–0.21%), Zr (205–240 ppm vs. 118–179 ppm), and Sr (253–301 ppm vs. 194–257 ppm) contents. With decreasing MgO, the Al_2O_3 and Na_2O contents increase and CaO, Cr, Ni, and V contents decrease. This is evidence that olivine and clinopyroxene deposited from melts with an insignificant fraction of plagioclase.

Following the same trend, the P_2O_5 content increases to 0.27% in sample S5328/4 and then sharply decreases to 0.13% in the lowest-magnesian basalt S5324/7, indicating deposition of apatite from the melt at the last stages of melt differentiation.

With decreasing MgO, TiO_2 contents first increase from 2.62% (sample S5332/1) to 3.16% (sample S5329/9) and then decrease to 2.17% in the most differentiated sample S5324/7. Together with TiO_2, Fe_2O_3 content also decreases. This indicates the deposition of Fe–Ti ore minerals from the melt at the late stages of Fe–Ti melt differentiation.

In the MgO–P_2O_5 diagram, the composition points of two large groups of volcanics form two fields with a distinct tendency of increasing P_2O_5 content with decreasing MgO content: lower (from 0.07 to 0.12%) and higher (from 0.10 to 0.17%) (see Fig. 4g).

The field of lower contents includes the composition points of varieties of different coherent groups, while the field of higher contents is formed mainly by volcanics of the main group, basalts of the high-Ti group, and some representatives of high-Al rocks (S5314/1, S5316/22, S5318/4, S5319/1, S5330/4, S5001/38, S5002/1,3,5,7, S5005/8). At the same time, the main part of high-Al volcanics forms a field of rocks with the lowest P_2O_5 contents (0.06–0.08%) (see Fig. 4g).

Obviously, among plagioclase phenocrysts in high-Al rocks with elevated P_2O_5 contents, P-enriched crystals predominate. Taking into account the fact that in these samples, xenocrysts prevail among phenocrysts; most likely, they are the source of additional phosphorus in these volcanics, because, as mentioned above, apatite inclusions occur in some xenocrysts.

In the MgO–V diagram, high- and low-Al rocks are clearly distinguished from the main part of basalts, respectively, by lower and higher V contents (see Fig. 4h). High-Ti basalts with higher V contents at the same MgO contents are also distinguished on this diagram.

Contents of Trace Elements in Studied Rocks

The behavior of trace elements in the studied basalts and dolerites was investigated on the basis of ISP-MS data and is presented in Supplement 1: Table S2.

The chondrite-normalized REE spectra in low- and high-K samples of coherent groups differ from each other in the LREE area. If the REE spectrum in low-K rocks decreases from Sm to La ($(La/Sm)_n$ 0.51–0.87), then it increases in most high-K samples ($(La/Sm)_n$ 0.95–1.62) (Figs. 5a, 5b).

This provides grounds to attribute low-K volcanics of coherent groups to depleted N-MORB-type oceanic tholeites, and high-K ones—to T-MORB tholeites.

In the HREE and MREE field, the spectrum of depleted rocks is more gentle ($(Sm/Yb)_n$ 0.99–1.25), while that of enriched rocks is steeper ($(Sm/Yb)_n$ 1.01–1.77), which indicates a greater generation depth of T-MORB melts. The spectra of more differentiated volcanics are located at a higher level, they have a negative Eu anomaly, indicating that plagioclase fractionation occurred in the differentiated melts.

The REE spectra of low-Al basalts regularly increase from HREE to LREE, and the increase in the LREE region is steeper than that in the enriched rocks

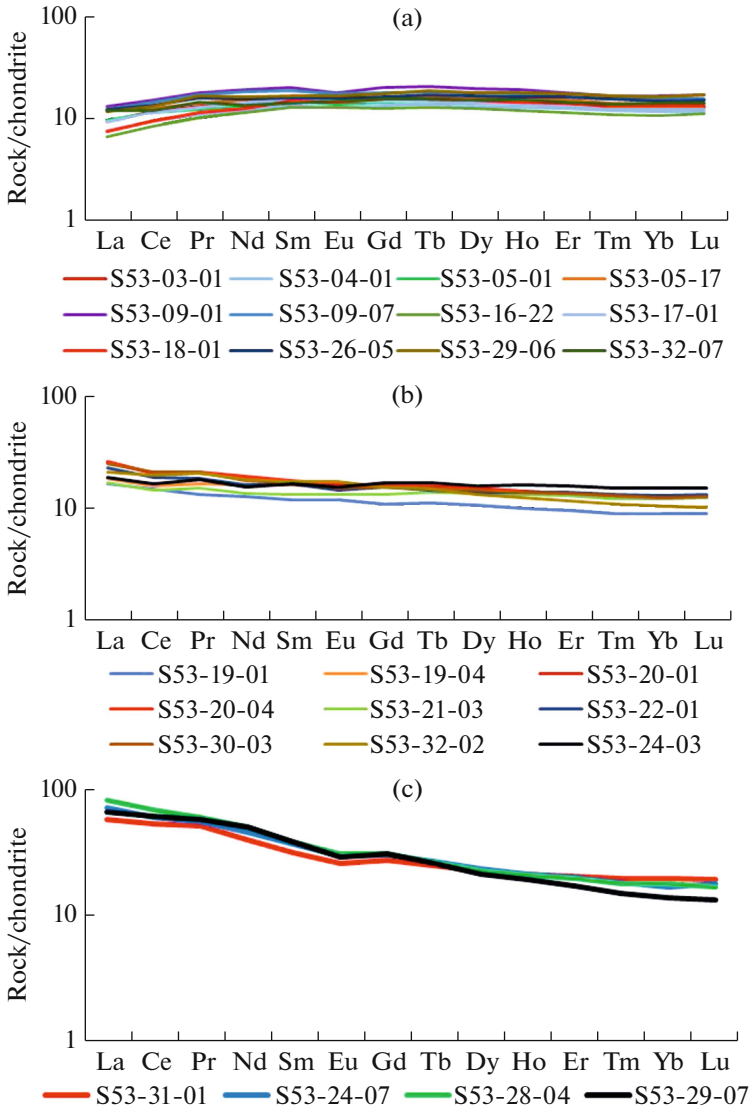

Fig. 5. Chondrite-normalized spectra of rare-earth elements of the studied basalts and dolerites (normalization was carried out according to [52]). (a–c) Tholeites: (a) N-MORB, (b) T-MORB, (c) E-MORB.

we have studied $(La/Sm)_n = 1.63–2.13$ and $(Sm/Yb)_n = 1.59–2.71$. This allows us to refer these volcanics to E-MORB tholeites (see Fig. 5c).

The $(Sm/Yb)_n$ values are lower than those of basalts melted at the garnet-facies depth. However, they noticeably exceed those of basalts generated at the spinel-facies depth [18]. This means that the formation of primary melts of low-Al volcanics occurred at a deeper level, intermediate between the spinel- and garnet-facies depths. A weak negative Eu anomaly is present on all spectra, indicating insignificant fractionation of plagioclase in melts.

The above subdivision of the studied rocks by the REE spectra pattern is also confirmed by the behavior of other trace elements, especially those that belong to the hygromagmatophilic ones, i.e., have affinity to the magmatic melt.

The lowest concentrations of these elements (ppm) in N-MORB tholeites are:

— La (2.13–5.15);
— Nb (1.45–4.33);
— Rb (0.65–4.84);
— Ba (7.6–29);
— Sr (103–157);
— Th (0.09–0.45);
— U (0.03–0.18).

On average, element contents are higher in T-MORB tholeites (ppm):

— La (3.05–8.64);
— Nb (2.90–11.08);

— Rb (2.42–10.73);
— Ba (29–89);
— Sr (125–200);
— Th (0.26–1.41);
— U (0.08–0.25).

Element contents are significantly higher in E-MORB volcanics (ppm):

— La (19–27);
— Nb (25–28);
— Rb (7–22);
— Ba (124–256);
— Sr (211–305);
— Th (1.65–2.81);
— U (0.41–0.72).

The ranges of Pb contents are approximately the same in most rock varieties: 0.20–0.86 ppm, and they are noticeably higher only in the E-MORB tholeites, 1.02–1.63 ppm. The ranges of Zr contents in basalts of coherent groups also coincide: 42–128 g/t, which are significantly higher in E-MORB rocks: 214–247 ppm.

The distinguished geochemical types of basalts and dolerites are distinguished by the character of spider diagrams. In the majority of N-MORB tholeites, the spectrum lines decrease beginning from Sm and further from La toward even more incoherent elements Nb and Th. This is reflected in the value of $(Nb/La)_n$ 0.68–0.89 and $(Th/Nb)_n$ 0.46–0.60 (Fig. 6a).

In typical depleted basalts, the spectrum line decreases further toward Ba and Rb. However, no such rock varieties have been found among the depleted tholeites of the Faraday Polygon area.

The spectrum lines of the studied rocks fell either to Ba $((Ba/Th)_n$ 0.52–0.87), then slightly rise to Rb $((Rb/Th)_n$ 1.06–1.55), or to Rb $((Rb/Th)_n$ 0.42–0.86) with a small positive anomaly of Ba $((Ba/Th)_n$ 1.07–1.44), or immediately rise to Ba and Rb.

As in typical depleted basalts, deep negative Pb and U anomalies are characteristic of most of the studied samples.

Sr shows relatively small negative anomalies or they are absent.

All depleted volcanics show a positive Zr anomaly $((Zr/Nd)_n$ 1.18–1.36) and a small negative Hf anomaly on spider diagrams.

The spider diagrams under consideration demonstrate that the widespread depleted tholeites of the studied MAR segment are enriched in Zr, selectively in Ba and Rb (Fig. 6a).

Single samples are enriched in:

— Nb (S5305/1, S5332/7 $((Nb/La)_n$ 1.02–1.06));
— Th (S5309/7 $((Th/Nb)_n$ 1.18);
— U (S5305/10,17, S5317/1, S5318/1 and S5329/3 $((U/La)_n$ 1.00–1.88));
— Pb (S5305/1, S5309/7, S5332/7).

The spider diagrams of T-MORB tholeites (see Fig. 6b) are very similar to those of N-MORB tholeites. Most of them are characterized by deep negative Pb and U anomalies and small negative Hf anomalies. Some samples show a weak positive Zr anomaly.

Sr varies within small limits, demonstrating the tendency to increase negative anomaly in adjacent spectra.

The specificity of T-MORB tholeites is that their spectra lines, having started to rise from Sm, continue to rise further from La to Nb $((Nb/La)_n$ 1.10–1.28). Their continuation towards even more incoherent elements is the same as in the depleted samples: the spectra lines fell towards Th $((Th/Nb)_n$ 0.58–0.69) and then again rise uniformly towards Ba and Rb.

The occurrence of a positive Nb anomaly on the spider diagrams of T-MORB tholeites indicates the involvement of HIMU mantle source material in their melting [54].

Some T-MORB tholeites are enriched in (Fig. 6b)

— Th (S5330/3 $((Th/Nb)_n$ 1,09);
— U (S5319/1, S5320/4, S5330/3 ((U/La)n 0.91–1.02);
— Pb (S5318/11, S5316/22 $((Pb/La)_n$ 0.78–1.28);
— Sr (S5332/2 $((Sr/Pr)_n$ 0.87).

The spider diagrams of high-Al volcanics are characterized by a small positive Sr anomaly $((Sr/Pr)_n$ 1–1.39) and a rise of the spectrum lines simultaneously to both Ba and Rb (see Fig. 6c).

Obviously, the occurrence of positive Sr anomaly, high position of the spectrum in the Ba and Rb area, is associated with a large number of plagioclase phenocrysts in the groundmass. In three studied samples (S5316/22, S5319/1, S5320/7), REE spectral lines in the Pb area lie higher, which is apparently associated with the presence of plagioclase xenocrysts, which may be Pb carriers.

Spider diagrams of low-Al basalts and dolerites differ from the above considered ones by significantly higher levels of the most hygromagmatophilic elements, from La to Rb. Their common features are the presence of deep negative Sr and Pb anomalies (see Fig. 6d).

The spider diagrams of samples S5331/1 and S5329/7 are close to each other: the spectrum curve rises from La to Nb $((Nb/La)_n$ 1.11–1.26) and then sharply falls toward Th $((Th/Nb)_n$ 0.58–0.59) and less sharply toward Ba $((Ba/Th)_n$ 0.91–0.93) and Rb.

This type of spectrum is characteristic of basalts, in the melting of which the HIMU mantle component is involved [54].

In sample S5328/4, the spectrum in the area of the most incoherent elements has a sawtooth profile formed by positive La, Nb, and Ba anomalies separated by negative U, Th, and Rb anomalies (see Fig. 6d).

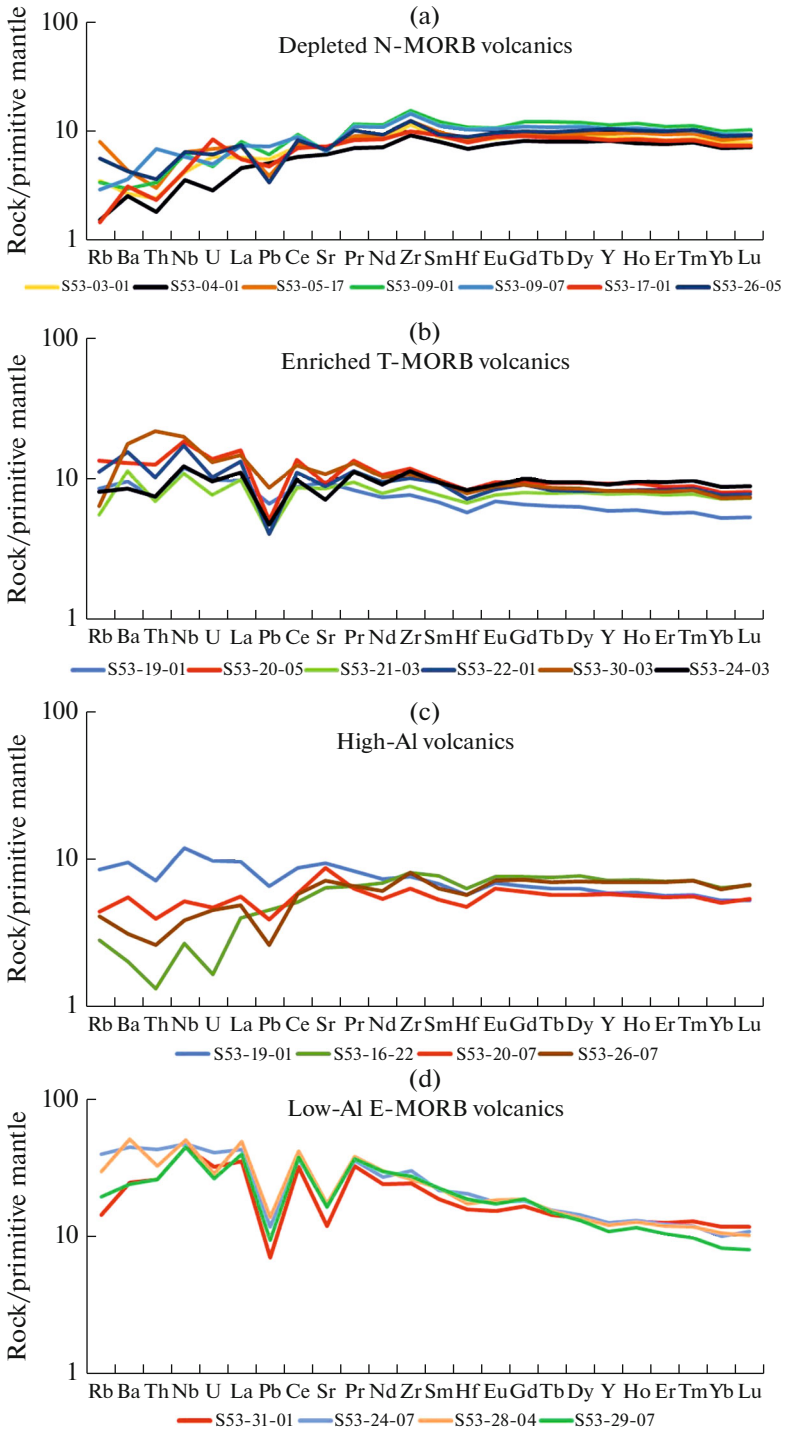

Fig. 6. Primitive mantle-normalized spider diagrams of trace elements of the studied basalts and dolerites (normalization was carried out according to [27]). (a) N-MORB tholeites; (b) T-MORB tholeiites; (c) high-alumina volcanics; (d) E-MORB tholeiites.

Sample S5324/7 has rare negative anomalies on the spectrum line in this region and a plateau in the interval from La to Rb (see Fig. 6d).

The spectra of volcanics of samples S5328/4 and S5324/7 indicate their involvement in the melting of the enriched EM-type mantle. It is evident, however, that the mantle from which each of these samples was derived had its own compositional features [54].

Let us consider some patterns of covariations of the contents of rock-forming oxides and trace elements.

Their contents were found to vary under the influence of two factors:

— the degree of melt differentiation;

— the degree of melt enrichment with lithophilic hygromagmatophilic elements.

To level out the influence of the degree of differentiation, we will operate with the $(La/Sm)_n$ ratio, i.e., the ratio of those elements that react to the processes of fractional crystallization of melts. Differences in their behavior are manifested at the latest stages of fractionation. These differences are characteristic only of low-Al rocks; they are not wide being in the range of $(La/Sm)_n$ = 1.76–2.17. In the diagram $(La/Sm)_n$–NB, N-MORB and T-MORB tholeiites are united in the variation diagram $(La/Sm)_n$ in a single narrow field in which Nb contents increase with increasing $(La/Sm)_n$ (Fig. 7a).

The composition points of low-Al E-MORB volcanics form an independent field, not adjusted to the previous one and located at a significantly higher level of weakly variable Nb values.

The subfields of depleted and enriched varieties are very extended, indicating a large variability of $(La/Sm)_n$ in both geochemical types. A similar distribution of samples is shown in the $(La/Sm)_n$–Ba diagram (see Fig. 7b).

The difference is that the Ba contents vary very strongly within the field of low-Al volcanics. In terms of Th and Sr contents, composition points of most samples form fields as in the case of Nb; in terms of K_2O, Rb, and U contents, it is as in the case of Ba.

However, single samples in these diagrams lie beyond the fields.

Samples of both depleted (S5003/25, S5005/13, S5305/17) and enriched tholeites (S5320/4) are characterized by higher Rb contents.

Sample S5320/4 is also characterized by higher K_2O content; the sample S5005/13 also has higher Sr contents.

The low-Al volcanic rock (S5331/1) fall out of its field due to significantly lower Sr values. The depleted basalt S5309/7, enriched volcanic rocks S5330/3, and low-Al high-K basalt S5324/7 are characterized by higher Th contents (see Fig. 7c).

Depleted samples S5317/1 and S5329/3 have higher U contents.

The similar distribution pattern of rock compositions is seen in $(La/Sm)_n$–Pb, P_2O_5 diagrams (see Fig. 7d).

In this case, however, in addition to those two fields present in all previous diagrams, another field was formed. It includes composition points of mainly depleted basalts with higher Pb and P_2O_5 contents at the same $(La/Sm)_n$ values. Furthermore, the trends of variations in their contents are extrapolated to the field of E-MORB volcanics.

Samples with higher Pb content were dredged from the rift valley throughout the studied MAR segment at stations S5303, S5304, S5305, S5307, S5309, S5316, S5317, S5318, S5003, and S5005, many of which also have P_2O_5 higher contents.

Samples S5318/11 and S5330/3 belong to enriched basalts with higher Pb and Th contents; samples S5314/1, S5319/4, and S5332/2 belong to those with higher P_2O_5 content.

In the $(La/Sm)_n$–Zr diagram, are three distinct fields of N-MORB, T-MORB, and low-alumina E-MORB varieties (see Fig. 7e).

The Zr contents in the depleted rock varieties are the same and even higher than in the enriched volcanics. The variation trend in the field of the depleted rocks is extrapolated to the field of low-Al basalts and dolerites.

There are several fields in the $(La/Sm)_n$–TiO_2 diagram: the E-MORB field, the field of N-MORB and T-MORB volcanics, tholeites enriched with lower TiO_2 contents at the same $(La/Sm)_n$ values (S5319/1, S5320/7, S5322/5), and two fields of depleted tholeites with successively higher TiO_2 contents at the same $(La/Sm)_n$ ratios. The latter two fields are made of composition points of high-Ti rocks and high-Ti high-Fe rocks (Fig. 7f).

In the $(La/Sm)_n$–Cr and Ni diagrams, the main group of samples forms three wide fields of N-, T-, and E-MORB volcanics, in which the contents of these elements decrease successively with increasing $(La/Sm)_n$ (see Fig. 7g).

Furthermore, composition points of some samples extend beyond these fields both toward higher and lower contents and form compact groups. Samples with higher Cr and Ni contents belong mainly to the depleted varieties and occur in all parts of the Faraday polygon area. In addition, the same samples often have lower Cr and Ni contents and most samples are confined to the area immediately south of the Charlie Gibbs FZ.

The following regularities have been revealed.

On variation diagrams with lithophilic trace elements, N-MORB, T-MORB, and E-MORB volcanics do not form a single field with a unified trend of N-MORB to E-MORB variations. The composition points of the latter in all diagrams form an independent field of the most enriched rocks (by the enrichment index $(La/Sm)_n$) with significantly higher contents of lithophilic elements; at the same time, they have a lower enrichment index $(Nb/La)_n$ in comparison with T-MORB-type volcanics (see Fig. 7h).

In the $(La/Sm)_n$–Nb, –Rb, –Ba, –Sr, –U, –Th, and $-K_2O$ diagrams, N-MORB and T-MORB tholeites form a single field in which the contents of these elements consistently increase with increasing $(La/Sm)_n$ ratio. This gives grounds to state that a series

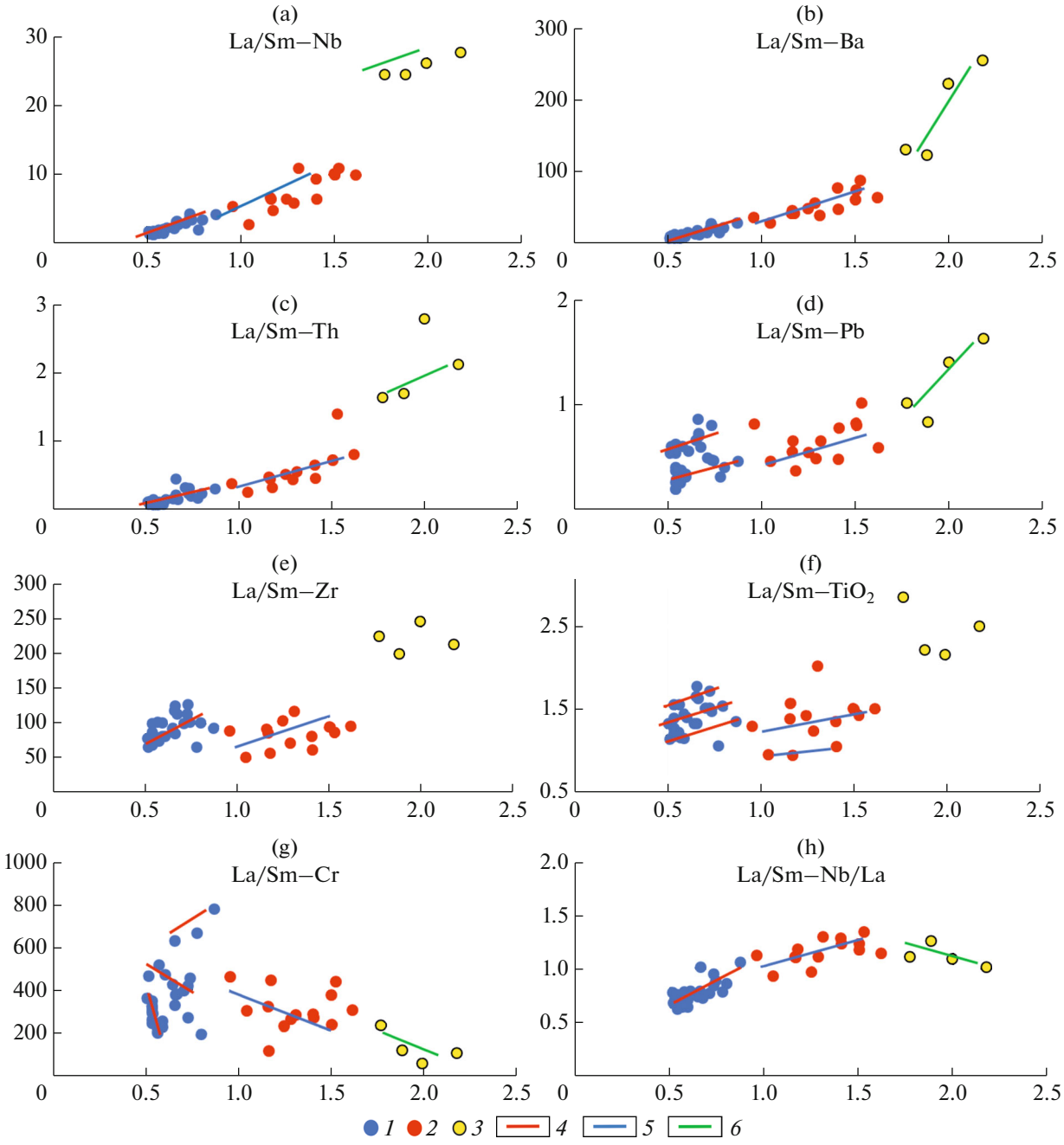

Fig. 7. Diagrams of variations in contents of rock-forming oxides (%) and some trace elements (ppm) depending on $(La/Sm)_n$ value in basalts and dolerites. (*1–3*) Geochemical rock types: (*1*) depleted N-MORB, (*2*) enriched T-MORB, (*3*) low-alumina E-MORB; (*4–6*) trends of rock variations in geochemical types: (*4*) N-MORB, (*5*) T-MORB, (*6*) E-MORB.

of these rocks was formed due to mixing two mantle components: depleted mantle and enriched mantle containing matter of the HIMU mantle source, as evidenced from the spider diagrams of T-MORB-type tholeites.

By contents of a number of elements, composition points of single samples go beyond this field towards higher values. In the $(La/Sm)_n$–Pb, $-TiO_2$, and $-P_2O_5$ diagrams, composition points of most samples are located beyond the unified field of N- and T-MORB tholeites, forming independent fields with a trend of variations falling into the field of E-MORB tholeites.

These facts indicate that the formation of N-MORB and T-MORB volcanics involved an additional component, which could be a substance similar to the mantle substrate in the composition. The latter was a source of E-MORB volcanics. This involvement had a selective character.

The $(La/Sm)_n$–Zr diagram shows that the N-MORB tholeites have higher Zr content than the T-MORB tholeites, which is not typical since these types of tholeites usually have opposite ratios.

All spider diagrams of the depleted basalts show a positive Zr anomaly. This is also not typical since a negative Zr anomaly is commonly observed.

The analysis confirms that the depleted mantle of the given MAR segment is enriched in Zr. Taking into account that the trend of variations in compositions of N-MORB tholeiite in this diagram is extrapolated to the E-MORB tholeiitic field, it is obvious that the enrichment could be the result of selective influence of the mantle substrate of these tholeiites.

Isotope Compositions of Samples

The measured $^{87}Sr/^{86}Sr$, $^{143}Nd/^{144}Nd$, $^{206}Pb/^{204}Pb$, $^{207}Pb/^{204}Pb$, and $^{208}Pb/^{204}Pb$ isotope ratios in studied basalts and dolerites are presented in Table 1. The studied samples include two T-MORB basalts (S5322/1 and S5330/3) and two low-alumina high-K E-MORB rocks: basalt S5324/7 and dolerite S5329/7. We also used published data on this area [44, 56, 58].

The analysis of the distribution of measured isotopic ratios on the variation diagrams shows that they lie in the field of Icelandic Rise. At the same time, some points in some diagrams lie in the overlap zone of the Icelandic and Azores fields [22] (Figs. 8a, 8d).

In the $^{206}Pb/^{204}Pb$–$^{207}Pb/^{204}Pb$ and $^{206}Pb/^{204}Pb$–$^{208}Pb/^{204}Pb$ diagrams, composition points of most studied and borrowed samples extend along the line connecting the DM and HIMU mantle sources. Furthermore, the largest proportion of the HIMU material is noted not in E-MORB-type low-Al volcanics but in T-MORB basalts (sample S5322/01). This is in agreement with the geochemical data indicating that the $(Nb/La)_n$ ratios, an indicator of the amount of HIMU end-member in tholeites, are also higher in T-MORB basalts (Figs. 8a, 8b).

Basalt of sample S5322/1 represents the end member of this field of isotope variations with the largest contribution of the HIMU component or it is the result of mixing of a depleted melt with that having an even larger proportion of the HIMU component. This sample was dredged from a large neovolcanic uplift (Segment 7) that formed in the southern part of the Faraday polygon area.

Other basalts dredged here (stations S5320–S5322) are geochemically similar to the latter. It is likely that material more enriched in HIMU component was not dredged. The $^{206}Pb/^{204}Pb$–$^{207}Pb/^{204}Pb$ and $^{206}Pb/^{204}Pb$–$^{208}Pb/^{204}Pb$ diagrams also show that the HIMU end member is also involved in the formation of E-MORB rocks but in smaller amounts.

In these diagrams, composition points of samples S5330/3 and S5324/7 are slightly shifted from the main group of samples towards the mantle sources EM-1 and EM-2. In terms of geochemistry, these samples are characterized by elevated Th contents (see Fig. 6).

The $^{206}Pb/^{204}Pb$–$^{143}Nd/^{144}Nd$ diagram shows that composition points of all volcanics, except for a few depleted basalts, deviate to some extent from the line of the mixing of DM and HIMU sources toward the mantle sources EM-1 and EM-2 (see Fig. 8c).

Considering the $^{87}Sr/^{86}Sr$–$^{143}Nd/^{144}Nd$ diagram, one can more definitely say that the studied basalts contain the EM-2 mantle component (see Fig. 8d).

All analyzed samples in this diagram form one elongated field, the trend of variations of which begins from the mantle source DM and crosses the line connecting the compositions of the HIMU and EM-2 mantle sources. The field is beyond the triangle with points of DM, HIMU, and EM-2 at the tops.

At the same time, the N-MORB depleted basalts are located closer to the DM point, T-MORB basalts are further away from it and, then, low-Al E-MORB volcanics. This distribution corresponds well to the geochemical variations of the basalt types under consideration.

Spatial Variations in Composition of Volcanics

The observed wide variations in the composition of volcanics mask the pattern of spatial variations in contents of most rock-forming oxides along the MAR axis. The latter is noted only for MgO, K_2O, and P_2O_5. We have analyzed these variations only for volcanics of coherent groups since the amount of low-Al rocks is insufficient for these purposes and the variations in the composition of high-Al volcanics depend on the amount of plagioclase phenocrysts.

In the latitude–MgO diagram is a distinct increase in maximum MgO contents north and south of a large neovolcanic uplift that formed at Segment 7 (48.41°–48.46° N) (Fig. 9a).

We have used the highest MgO values for comparison because they are characteristic of the least differentiated volcanics. In the northward direction, there is a very sharp increase in MgO contents along Segment 7 from 5.24 to 7.60% and then gradually to 8.29% at the Charlie Gibbs FZ.

Against the general increasing MgO values, its content decreases to 6.06 and 7.16% at Segments 6 and 2, respectively. These sites have the lowest upper mantle temperatures for this MAR segment and, accordingly, the lowest degrees of partial melting, which (according to [31]) leads to decrease in MgO contents in primary basaltic melts.

High-Na basalts, which are also indicators of lower degrees of partial melting, are also common at Segment 2.

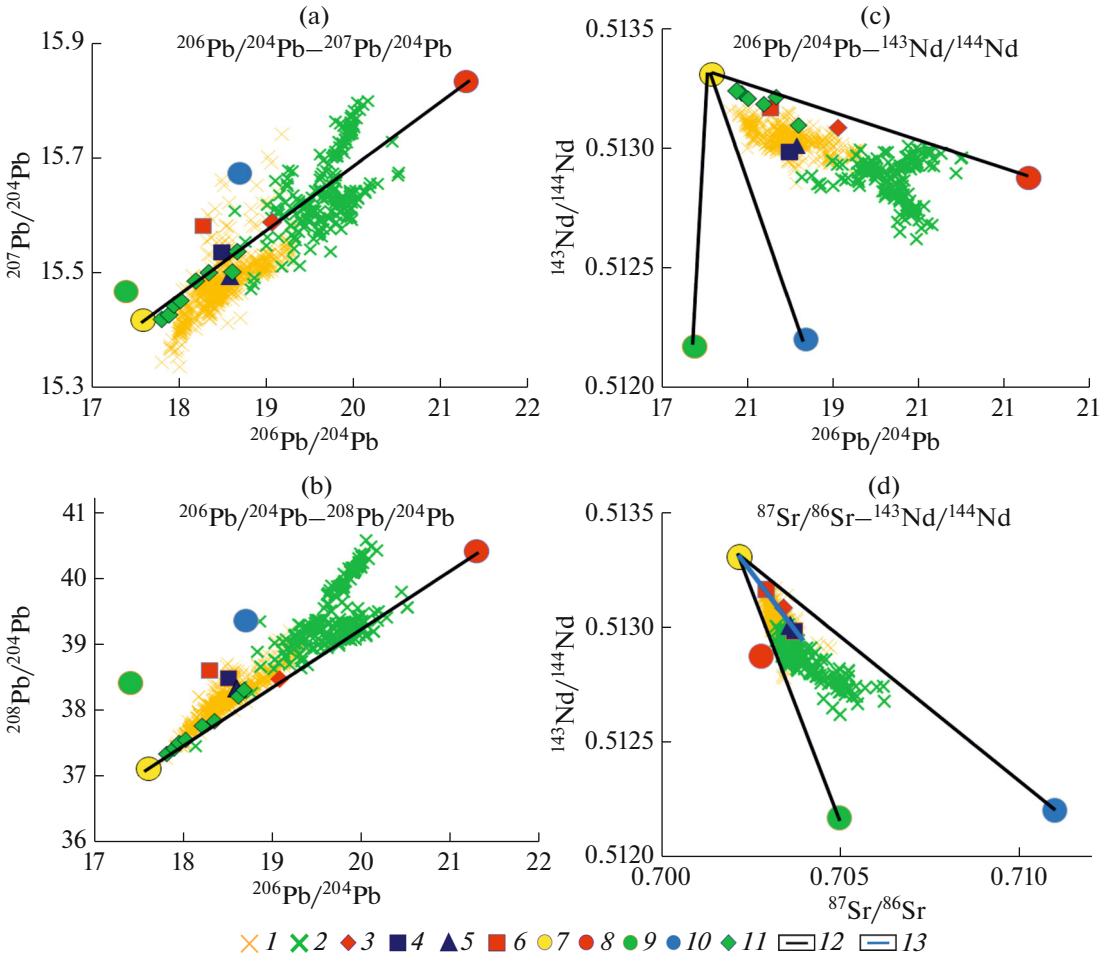

Fig. 8. Diagrams of variations of isotope ratios $^{87}Sr/^{86}Sr$, $^{143}Nd/^{144}Nd$, $^{206}Pb/^{204}Pb$, $^{207}Pb/^{204}Pb$, $^{208}Pb/^{204}Pb$ in basalts and dolerites. (*1–2*) Basalts: (*1*) Iceland Rise (after [22]), (*2*) Azores Rise (after [22]); (*3–6*) sample: (*3*) S5322/1, (*4*) S5324/7, (*5*) S5329/7; (*6*) S5330/3; (*7–10*) mantle source: (*7*) DM (after [25, 28]), (*8*) HIMU (after [25, 28]), (*9*) EM-1 (after [25, 28]), (*10*) EM-2 (after [25, 28]); (*11*) basalts of the MAR segment (according to GEOROC [22]); (*12*) lines connecting the compositions of mantle sources; (*13*) the trend of variation in isotopic compositions of the studied samples.

However, lower MgO contents are characteristic not only of volcanics distributed in the areas of lower upper mantle temperatures. By all signs, the area of a large neovolcanic rise at Segment 7 is distinguished as the area of higher upper mantle temperatures, where occur rocks with the lowest MgO contents. Obviously, the basalts of the neovolcanic rise were melted from a less magnesian substrate. Furthermore, as shown by the long-axis variations in MgO contents, the proportion of this substrate decreases in the zone of melting from south to north.

The along-axis variations in Cr and Ni contents repeat those obtained for MgO but, unlike the latter, there are points irregularly distributed along the entire profile, where volcanics with anomalously high Cr values (603–976 ppm), accompanied by elevated Ni contents (176–181 ppm), are found. Obviously, melting of the substrate enriched in Cr and Ni occurred at these points.

Along-axis variations in K_2O and P_2O_5 contents have a close distribution pattern, opposite to that for MgO.

We have analyzed the latitude–K_2O diagram (Fig. 9b). For this purpose, we have used the lowest K_2O values because they are characteristic of the least differentiated melts.

The highest K_2O values (0.32%, reaching 0.51% in the most differentiated melts) are observed in the area of a large neovolcanic uplift formed at Segment 7 (48.41°–48.46° N).

They decrease sharply to 0.18% to the north along Segment 7 and then gradually to 0.08%. However, from the northern boundary of Segment 1 to the Charlie Gibbs FZ, they gradually increase again to 0.10% (0.16% in the most differentiated varieties).

Against the background of a gradual decrease in K_2O content from south to north, one can observe bursts of K_2O contents at Segments 1 and 3. This can

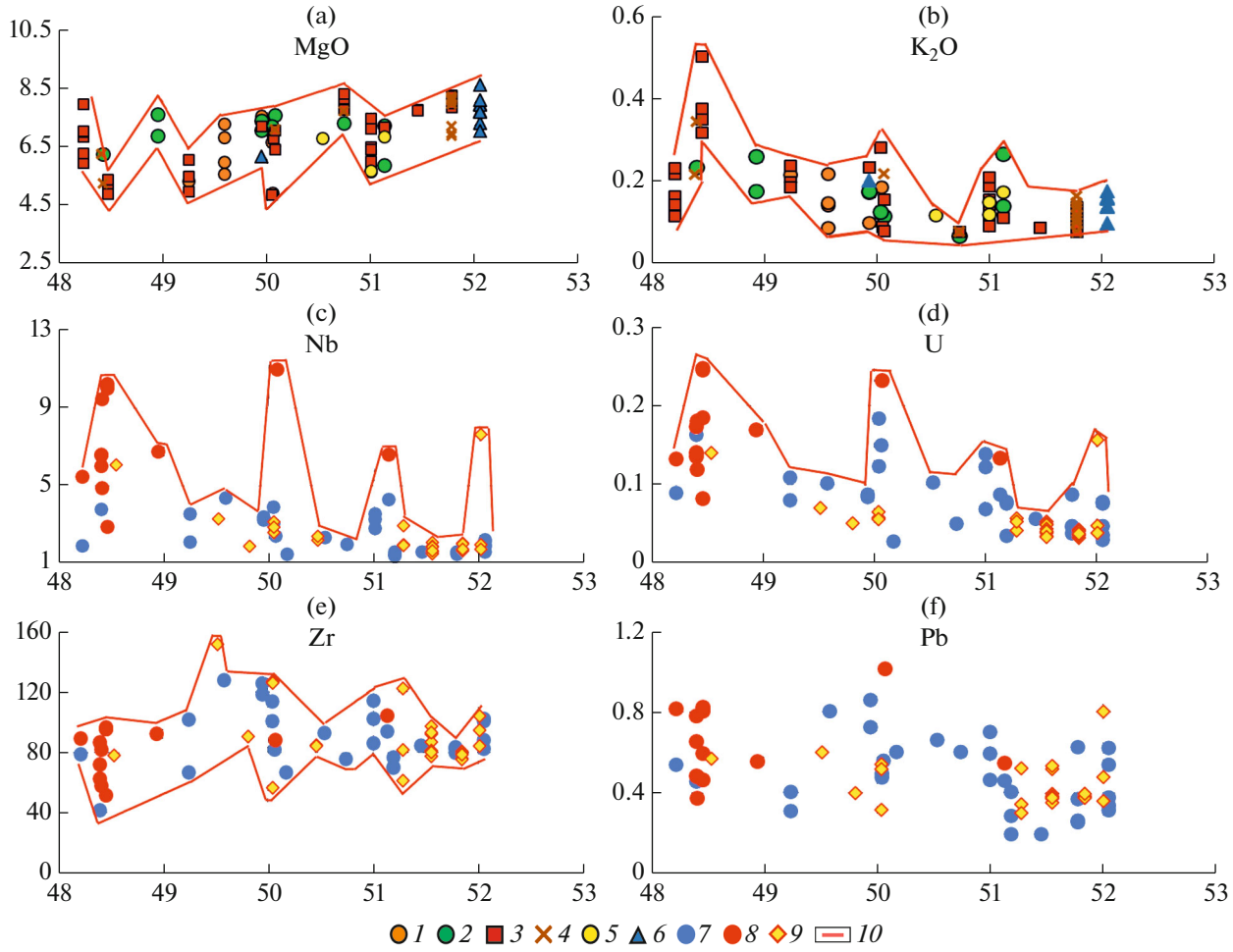

Fig. 9. Along-axis variations in MgO and K_2O (%), Cr, Nb, Zr, and Pb (ppm) contents in basalts and dolerites in the MAR segment between the Charlie Gibbs and Maxwell fracture zones. The degrees of north latitude are shown along the abscissa. (*1–5*) Petrochemical groups: (*1*) high-Ti, high-Fe, (*2*) high-Fe, (*3*) main, (*4*) high-Ca, (*5*) high-Na; (*6*) high-Ti; (*7–10*) geochemical types: (*7*) N-MORB, (*8*) T-MORB; (*9*) samples (from the GEOROC database [22]); (*10*) lines bounded the lower and upper limits of variations in contents of MgO, K_2O, and Zr and the upper limits of variations in contents of Nb and U.

be due to the occurrence of T-MORB volcanics on rises occurring in the crestal zone.

The pattern of long-axis variations in the majority of studied lithophilic elements is close to that for K_2O and P_2O_5. As in K_2O and P_2O_5, they vary over a very wide range in the neovolcanic rise area at Segment 7.

In the latitude–Nb diagram, the highest Nb contents (10 ppm) are characteristic of the basalts of the large neovolcanic rise formed at Segment 7 (see Fig. 9c).

In the northern direction, they decrease sharply to the northern boundary of Segment 6 up to 3.5 ppm, and then gradually to the Charlie Gibbs FZ up to 1.7 ppm, increasing near the FZ to 2.2 ppm.

High-amplitude bursts of Nb values (up to 6–11 ppm) are observed in the vicinity of Segments 1 and 3, as well as directly near the Charlie Gibbs FZ, because basalts are developed in these sections among other rocks T-MORB.

A small burst (up to 4.5 ppm) is also observed in the area of Segment 5, but N-MORB basalts have an elevated Nb content here.

The behavior of La, Ba, Rb, U, Sr, and Th is practically the same. Furthermore, in the area of Segments 1 and 3, along with T-MORB basalts, N-MORB basalts enriched in these elements (especially U) are also common (see Fig. 9d).

Zr has a different pattern of variations (see Fig. 9e).

The Zr values and the range of its variations throughout the studied MAR segment vary slightly (41–104 ppm) and coincide in depleted and enriched volcanics. However, in the high-relief area at Segments 1, 3, and 5, there are many rocks with noticeably higher Zr contents (114–152 ppm) with depleted rock varieties predominating among them (see Fig. 9e).

Pb has a complex pattern of variations (see Fig. 9f).

In spite of very wide variations in Pb values, it is possible to note a tendency of their decrease from the large neovolcanic rise to the north from 0.38–0.81 to 0.20–0.63 ppm. Against the background of this decrease, basalts with higher Pb content (0.73–1.02 ppm), especially abundant in high-relief areas, with N-MORB basalts predominating among them are found in the northern part of the studied MAR segment up to 49° N.

Thus, among the volcanics of coherent groups are the differences with the highest contents of lithophilic elements localized in the area of a large neovolcanic rise at Segment 7. With rare exceptions, only T-MORB basalts are widespread here. The contents of lithophile elements in the volcanics drop sharply in the northern direction and then gradually decrease until the Charlie Gibbs FZ. Contents of some of them (K_2O, P_2O_5, Nb, La) increase slightly in the near-fault area.

Contents of lithophilic elements are also sharply lower in basalts distributed south of the neovolcanic uplift (see Fig. 9).

These observations suggest that the mantle substrate enriched in lithophilic elements melts beneath the MAR axial part in the area of the large neovolcanic rise at Segment 7. The volume of the substrate in the melting zone first sharply and then gradually decreases to the north.

According to geochemical and isotope data, the matter of the HIMU mantle source plays an important role in the composition of this mantle substrate along with the depleted mantle. This mantle substrate also has lower MgO, Cr, and Ni contents. T-MORB tholeiites show wide compositional variations in all components. This means that, in accordance with our analysis of covariance of geochemical parameters, the N-MORB and T-MORB tholeiitic melts are mixed in different proportions (see Fig. 7).

North of the neovolcanic rise, N-MORB volcanics derived from the depleted mantle are predominantly distributed. Furthermore, however, they also contain HIMU component matter, the proportion of which decreases to the north.

Beyond Segment 7, T-MORB tholeites are rare on rises formed in high-relief areas, where low-Al E-MORB rocks are also common. Geochemically, these T-MORB tholeiites are characterized by higher Sr content, while sample S5330/3 by Sr, Th, Pb, and Ba. According to isotope data, the same sample reflects a greater contribution of EM-2 mantle source material in its composition compared to basalts of neovolcanic and other rises at Segment 7.

In the high-relief areas, the depleted volcanics are selectively enriched in various lithophilic elements, which were discussed in more detail in the previous sections. In the northern part of the studied MAR segment, Pb-rich depleted volcanics are widespread, while locally are rocks with elevated Cr and Ni contents.

DISCUSSION

Possible Reasons for Diversity in the Composition of Volcanics

The analysis of variations in the composition of basalts and dolerites dredged in the studied area allowed us to unite them into several petrochemical groups. Some of them form a cluster of coherent groups. The elongated composition fields of volcanics of these groups on the MgO–oxide variation diagrams have subparallel trends of variation (see Fig. 4).

Among them are the main group of volcanics, which unites rocks with moderate contents of rock-forming oxides and groups of high-Ca, high-Na, high-Ti, high-Fe, and high-Ti high-Fe volcanics. Compared to the volcanics of the main group, the latter have higher CaO, Na_2O, TiO_2, and Fe_2O_3 contents, simultaneously TiO_2 and Fe_2O_3, respectively, at the same MgO values.

The trends of variations in contents of rock-forming oxides and trace elements in each group are close and have the following pattern. Contents of Fe_2O_3, TiO_2, Na_2O, K_2O, P_2O_5, V, lithophilic trace elements–lanthanides, Zr, Sr, Rb, Ba, and Nb increase with decreasing MgO content and CaO, Cr, and Ni contents decrease; there is a weak tendency to increase in Al_2O_3 content.

Such a pattern of variations reflects the process of fractional crystallization of primary basaltic melts, from which olivines, plagioclases, and clinopyroxenes crystallize during their ascent. The crystallization of these minerals leads to the depletion of the residual melt in Mg, Ca, Cr, and Ni and the successive enrichment in Fe, Na, Ti, P, and hygromagmatophilic elements.

REE spectra and spider diagram lines of less magnesian, i.e., more differentiated rocks occupy a higher level compared to more magnesian varieties and have negative Eu anomalies on REE spectra and Sr anomalies on spider diagrams. The latter confirms the fractionation of plagioclase in their melts.

In the MgO–oxide diagrams, a separate extended field, not parallel to the fields of coherent groups, is formed by composition points of a group of low-Al rocks combining basalts and dolerites (i). At similar MgO values, the latter are sharply different from other volcanics in lower Al_2O_3, CaO, SiO_2, Na_2O, Cr, and Ni contents and higher contents of TiO_2, Fe_2O_3, K_2O, P_2O_5, V, and lithophilic impurity elements (ii). With decreasing MgO values, the Al_2O_3 and Na_2O contents increase and the CaO, Cr, Ni, and V contents decrease, indicating the deposition of olivine and clinopyroxene from their melts with a small fraction of plagioclase (see Fig. 4).

Nevertheless, the crystallization of plagioclase is also indicated by negative Eu and Sr anomalies in their REE spectra and spider diagrams, respectively. The

sharp decrease in P_2O_5, Fe_2O_3, and TiO_2 contents in the least magnesian samples indicates the crystallization of apatite and Fe-Ti ore minerals from the melt at the last stages of melt differentiation of rocks of this group. The presence of highly differentiated samples among low-Al rocks indicates a prolonged ascent of their melts.

The degree of the saturation of the studied volcanics with plagioclase phenocrysts has a significant influence on their composition. Abundant plagioclase porphyritic basalts and dolerites form separate fields of high-Al rocks on MgO–oxide variation diagrams (see Fig. 4).

Within this group, variations in the composition of volcanics are caused by variations in the number of plagioclase phenocrysts; the more of the latter, the higher the Al_2O_3 content and the lower the contents of other oxides. This dependence is less pronounced for K_2O, P_2O_5, and most of the trace elements, which occur in small amounts in volcanics. At the same time, high-Al rocks differ from volcanics of coherent groups in higher Sr content, which increases with increasing Al_2O_3 content; their spider diagrams demonstrate positive Sr anomalies.

Some samples of this group are also distinguished by higher P_2O_5 and Pb contents, which is most likely due to the presence of large amounts of xenocrysts. Among the group of high Al volcanics are also aphyric varieties, which, in all parameters and their variations do not differ from plagioclase porphyritic rocks.

In this connection, we assume that the development pattern of aphyric varieties of high-Al basalts during the uplift to the surface was as follows: the accumulation and then dissolution of plagioclase phenocrysts in the melt.

The presence of several petrochemical groups of volcanics with similar pattern of fractionation indicates that the differences in the melting conditions of primary melts are also among the reasons that led to diversity of their compositions. The volcanics of the main group, which are widespread throughout the study area, represent all the variety of tested morphostructures and most often occur together with basalts of other petrochemical groups.

This gives us grounds to consider basalts of this group as a specific standard of typical melting conditions characteristic of this MAR segment, which took place at moderate temperatures, pressures, and degree of partial melting.

In accordance with experimental data on the melting of oceanic tholeiites under conditions characteristic of the spinel facies of the mantle depth [31] and observations of variations in the composition of basaltic glass along the MAR [32], a decrease in the degree of partial melting of the mantle substrate due to a lower melting temperature leads to an increase in the Al_2O_3, Na_2O and TiO_2 contents in the melts, and, on the contrary, an increase in the degree of partial melting due to a higher temperature leads to an increase in the CaO and MgO contents in the melts.

Consequently, the primary melts of the recognized volcanics of the high-Na and high-Ti groups were melted at lower temperatures and lower degrees of partial melting in comparison with the melts of the rocks of the main group, which is confirmed by the pattern of the spatial distribution of these volcanics.

The largest amount of high-Na volcanics was found at the low-relief Site 2 and near the Charlie Gibbs FZ. Samples free of rocks of other groups were dredged only at station S5303, which is located at one of the deep rift depressions.

The low relief is an indicator of low temperatures in the upper mantle beneath the MAR axis [32]. At station S5005, located at the junction of the rift valley with the Charlie Gibbs FZ, high-Na basalts were dredged together with high-Ti basalts. This is an area where a large transform fault provides a cooling effect [33].

In accordance with the above, the primary melts of the high-Ca rocks melted at higher temperatures and degrees of partial melting compared to the melts of the volcanics of the main group. This is also confirmed by the pattern of the spatial distribution of these volcanics.

They occur in small amounts but are widespread throughout the study area, being confined exclusively to ocean floor uplifts:

— stations S5321 and S5322, the large axial volcanic rise at Segment 7;

— station S5330, a major rise on the western flank of Segment 5;

— station S5304, an rise separating deep rift basins in Segment 2;

— station S5003, an axial rise in the central part of a spreading cell at the site south of the Charlie Gibbs FZ.

In other areas of the Atlantic, high-Ca basalts are also most common in the central parts of spreading cells [7]. Thus, high-Ca rocks are associated with uplifts of rift valley bottom. The latter are formed in centers of magmatic activity above the apical parts of rising diapirs of asthenospheric mantle, which are characterized by higher temperatures compared to other parts of the axial spreading zone [1, 17, 33, 42].

Basalts of the high-Fe group occur together with high-Ca samples. Compared to rocks of the main group, in general, they are characterized by higher CaO content and lower Al_2O_3 and Na_2O contents at the same MgO values (see Fig. 4).

These data indicate that high-Fe basalts were melted under higher temperature conditions at a higher degree of partial melting in areas of high magmatic activity.

In agreement with experimental data [31] and observations over variations in basaltic glass composition along the MAR [32], Fe_2O_3 contents in basaltic

melts increase with increasing melting depth. Thus, high-Fe basalts represent deeper derivatives of a rising diapir of the asthenospheric mantle.

At the same time, the level of depth of their melting does not fall below the spinel facies of depth. This is evidenced by the subhorizontal pattern of the REE spectrum in these basalts in the HREE and MREE areas (see Fig. 5).

Low-Al basalts and dolerites are distributed mainly in high-relief areas where the rift valley is orthogonal to the spreading axis and has a structure characteristic of typical spreading cells (Segments 1, 3, 5, 7).

They were dredged from large rises and ridges in the crestal zone (stations S5328, S5329, S5331, S5332) and they were dredged from the side of the rift valley only at Segment 7 (station S5324). In these morphostructures, other types of volcanics are distributed together with low-Al basalts and dolerites, being more representative.

Therefore, melting at these sites occurred both under the conditions most typical for this MAR segment and under significantly different conditions. Significantly higher values of the $(Sm/Yb)_n$ ratio (2.1–2.74) in these volcanics indicate their melting at a greater depth at a level intermediate between the garnet and spinel depth facies of the upper mantle. Obviously, this circumstance affects the composition of primary melts of volcanics, but the geochemistry and isotopic data of these rocks indicate a different composition of the melting substrate of these volcanics. According to the isotopic data, it is a mixture of three mantle sources: dominant DM, EM-2, and, to a lesser extent, HIMU.

This means that, in this area, the substance from the mantle sources EM-2 and HIMU occur in the depleted mantle (mantle source DM). Low-Al volcanics differ from all basalts of coherent groups in significantly higher REE, Nb, Rb, Ba, Sr, Th, Pb, and U contents.

The substrate of the HIMU mantle source could be oceanic crust that sank into the mantle in subduction zones, reached the core–mantle boundary, and then ascended as a plume (recycled oceanic crust) [50, 55, 59].

Typical derivatives of this mantle source in the Atlantic are volcanics of St. Helena Island. In volcanics of the Icelandic and Azores rises, the depleted mantle substance is largely present along with the component [51].

The origin of the substance of the EM-2 component is not so unambiguous. A number of researchers [27] consider it to be a derivative of recycled oceanic crust with admixture of the terrigenous material. In turn, according to [28, 30], recycling of continental crust takes place. At the same time, according to [39], the appearance of continental crustal matter in the melting zone of MORB basalts is associated with the detachment of its blocks in the subduction zone and their uplift directly to the melting zone.

Many researchers emphasize the important role of sources of processes of metasomatic alteration of continental mantle in the formation of EM mantle, occurring under the influence of either alkaline-silicate (EM-1) or carbonatite melts (EM-2) [2, 29, 43]. Such metasomatically altered mantle could appear in the melting zone beneath the axial spreading zone as a result of its tectonic delamination during continental rifting [34].

Based on the petrogeochemical and isotopic data we have obtained the substance of the EM-2 mantle source represents the transformed continental lithosphere. Taking into account the mosaic distribution pattern of low-Al volcanics, the continental lithosphere is present in the asthenospheric mantle in the form of blocks comparable in size to the occurrence areas of low-alumina basalts and dolerites (30–40 km across) and is located in the intermediate layer between the spinel and garnet facies of depth.

It should be noted that the substrate, the melting of which led to the formation of low-Al volcanics, is heterogeneous in composition. It follows from the fact that high-K and low-K varieties are distinguished among them. The high-K rocks of this group have higher P_2O_5, Zr, Sr, La, Nb, Rb, Ba, Th, and U contents. In addition, they are also heterogeneous in composition, being different in Rb, Ba, Sr, and Th contents. Based on geochemical parameters, the low Al volcanics are classified as E-MORB-type oceanic tholeiites.

The spatial distribution of high-Ti high-Fe basalts correlates with that of low-Al volcanics. They are similar in composition and are characterized by the highest TiO_2, Fe_2O_3, P_2O_5, and Zr contents and the lowest Al_2O_3 and CaO contents among the rocks of coherent groups. According to the geochemical features, they belong to the N-MORB oceanic tholeiites. Taking the spatial and petrogeochemical proximity of these basalts to low-Al rocks into account, it is obvious that the observed peculiarities of their composition are determined by the participation in their melting of the substance that was the protolith of low-Al basalts, dolerites, and, possibly, their low-K varieties.

The melts of high-Ti high-Fe basalts were melted at the level of the spinel facies of the upper mantle ($(Sm/Yb)_n$ approximately 1). This means that the continental lithosphere blocks extend vertically downward from the spinel depth level to intermediate depths between the latter and the garnet depth facies.

The peculiarities of the melting substrate composition are also reflected in the composition of volcanics of coherent groups, which are divided into low-K and high-K. The latter are also characterized by elevated P_2O_5 content.

As evidenced from the geochemistry and isotopy of rocks, the low-K varieties belong to oceanic N-MORB tholeites and were melted from the mantle substrate whose composition is close to the mantle source DM. The high-K varieties are T-MORB tholeites, which were melted from a substrate that is a mixture of three mantle sources: predominant DM, HIMU, and small amounts of EM-2.

Geochemically, they are distinguished from low-K rocks in higher La, Nb, Rb, Ba, Sr, Th, and U contents. Analysis of spider diagrams of N-MORB tholeiites showed that they are selectively enriched in Ba and/or Rb throughout the studied area, and some samples of this type are also enriched in such elements as Nb, Th, U, and Pb. Furthermore, their contents are generally lower than those in enriched varieties (see Fig. 6).

Thus, the diversity in compositions of the studied volcanics is determined by the following processes and factors:

— fractional crystallization of melts during ascent to the surface;

— accumulation of phenocrysts in melts;

— conditions of melting of primary melts (temperature, depth, degree of partial melting);

— heterogeneity of the melting substrate composition.

Inhomogeneities in the Composition of the Mantle Substratum of Volcanics

Based on isotopic data, the depleted mantle (mantle source DM) is considered the dominant mantle substrate from which the studied volcanics were melted. The substance of mantle sources HIMU and EM-2 played the subordinate role; the presence of the latter determines the inhomogeneities of the upper mantle composition.

The presence of HIMU mantle source is associated with deep mantle plumes containing the recycling oceanic crust. In our case, the scale of involvement of the HIMU component is incomparably small compared to large provinces of enriched basalts in the Atlantic, where the influence of plumes is expected.

However, there are also many examples of small local mantle inhomogeneities in the MAR crestal part with composition close to the HIMU mantle source. The prevailing insight into the origin of these inhomogeneities is that they are so-called passive chaotically distributed inhomogeneities in a convecting mantle enriched with incompatible elements and radiogenic isotopes [3, 11, 43, 49].

In particular, such inhomogeneities with markers of the HIMU mantle source matter may be associated with small portions of the material that detached from the plume and remained in the mantle for a long time until they entered the melting zone [13, 49]. In addition, in accordance with [20, 24], during melting of the material of the spreading plume head, the resulting melts can be trapped in the surrounding mantle in the form of veins and schlirs, leading to its contamination with the plume material.

However, our studies rather indicate that the mantle inhomogeneity identified beneath the neovolcanic rise at Segment 7, in the formation of which the HIMU component was involved, is not passive but active, i.e., we deal with a kind of microplume.

This is evidenced by two facts.

• The lowest Bouguer anomaly values in the entire Segment 7 area indicate an elevated temperature in the mantle and/or high intensity of melting, which led to increased crustal thickness.

• A sharp at first, then gradual decrease in the content of lithophilic elements in the volcanics in a northerly direction indicates the existence of an enriched mantle layer and its depletion in the same direction. This indicates that this layer is along-axis sublithospheric subhorizontal flow of hotter and enriched mantle moving northward and reaching the Charlie Gibbs FZ.

The southward direction of flow is ambiguous because only the Segment 8 area adjacent to the neovolcanic rise has been studied. As the mantle material moved and melted, it became depleted in lithophilic elements and enriched in refractory elements. Accordingly, new portions of melt at a distance from the microplume were less enriched in lithophilic elements but more enriched in MgO, Cr, and Ni. The existence of such a flow is also indirectly evidenced by the lowering of the relief of the axial and crestal zones in the low-relief areas from south to north.

In accordance with the transverse size of the neovolcanic rise at Segment-7, such a microplume is approximately 20 km across. Signs of similar subaxial subhorizontal flows of enriched mantle material of close scale (first hundreds of kilometers) are also present in other areas of the Atlantic. Among them are the MAR section between the São Paulo and Strakhov FZs in the northern part of the Equatorial Atlantic [7]. Here, the flow moves from the Sierra Leone plume, which is located near the MAR axial zone near latitude 1.7° N [45].

This plume is fading and small in size; to date it is actually a microplume. A second example is the MAR segment between the Bode Verde and Ascension FZs in the southern part of the Equatorial Atlantic [7], where a branch from the St. Helena plume located approximately 400 km east of the MAR axis serves as the microplume [46].

The origin of the microplume in the studied MAR segment remains to be determined in further studies. In our opinion, it may be one of the small branches of the Azores plume, the presence of which north of the Azores Rise is suggested in [56, 58]. One can also expect that this is another, already fading plume. In par-

ticular, there was a previously active plume in this region, with which the Milne hot spot was associated [57]. There is another point of view on the origin of microplumes, based on the fact that structures similar to the neovolcanic rise at Segment 7 and composed of enriched basalts appear with a regularity of 350–400 km along the MAR axial part within the South and Central Atlantic [7, 8].

This phenomenon is explained [7, 8] by the proposed existence of a system of cylindrical convective cells with an average diameter of 350–400 km along the MAR axis. The ascending branch of the asthenospheric mantle passing along the axis of the cylinder captures lumps of enriched material from the base of the upper mantle, where the matter with the characteristics of the HIMU mantle source can be concentrated. It is possible that the ascending branch of one of these cylindrical convective cells is located beneath the neovolcanic rise of Segment 7.

Earlier, considering the versions of the possible origin of the EM-2 mantle source, we came to the conclusion that the substance of this mantle source beneath the studied MAR segment is most likely represented by blocks of transformed continental lithosphere enclosed in the depleted mantle, i.e., these are typical passive mantle inhomogeneities. The continental lithosphere blocks may be captured by the asthenospheric mantle during its tectonic delamination at the stage of continental rifting [34].

In our case, however, another mechanism is preferable. It was proposed to explain the very diverse composition of basalts distributed to the south of the Atlantic's largest Romanche FZ [6]. This mechanism is based on the assumption of tectonic erosion of the thick continental lithosphere, which bordered with the asthenospheric mantle of the adjacent ocean basin along a long transform fault at the initial stages of oceanogenesis. The asthenospheric oceanic mantle was at the nearly the same depth level as the continental lithosphere and disintegrated it into separate blocks that were involved in the convecting oceanic mantle.

This process is likely for the Charlie Gibbs FZ, which has a long offset. The longer the offset, the longer the contact between continental lithosphere and oceanic subaerial asthenosphere at the initial stages of the opening of an ocean. Involvement of the substance of these continental lithosphere blocks in the melting process led to the formation of E-MORB tholeites.

Possible Scenario of Oceanic Crust and Bottom Structure Formation in the Studied MAR Area

When developing a possible scenario for the formation of oceanic crust in the studied MAR area, covering the Faraday polygon area and the near-fault area south of the Charlie Gibbs FZ, we have relied on the results obtained by analyzing the tectonic structure of this segment, the melting processes of basalts and dolerites that led to their observed rock diversity, the inhomogeneity of the mantle substrate of volcanics, and the relationships between different types of volcanics and ocean floor structures.

The study has shown that there is no direct influence of the Azores and Iceland plumes on the processes of crustal axial accretion in this MAR area. This area is distinguished by the lowest relief in the entire space between the Azores Rise and Icelandic Rise, which also indicates the lowest temperature of the upper mantle beneath this area.

Structurally, this is expressed in the extensive development of deep rift basins separated by small neovolcanic ridges and the predominance of low ridges in the crestal zone; compositionally, in the distribution of high-Na basalts in these areas.

Against this background, the high-relief areas with typical spreading cells orthogonal to the spreading axis are anomalous in contrast to the low-relief areas with structures predominantly oblique strike to the spreading. The formed spreading cells indicate focused upwelling (diapirism) of the asthenospheric mantle, which is absent in the case of echeloned development of deep rift basins.

The high-relief areas have different origin and structure. In the south of the study area at Segment 7, the high-relief structures are of volcanic origin: a large neovolcanic rise in the axial zone and large rises on the eastern flank composed of basalts similar to those of the neovolcanic rise. This is the most powerful center of magmatic activity in the studied MAR region.

In the north of the Faraday polygon area at Segment 1, the high-relief structures are of tectonic origin. These are oceanic core complexes with a widespread distribution of gabbroids and serpentinized ultramafic rocks. At the more southern Segment 3, oval rises occur on the eastern flank, which are tectonic structures that were uplifted as a result of serpentinization of ultramafic rocks; on the western flank are complementary former neovolcanic rises.

The tectonic structures studied at Segments 1 and 3 are indicators of reduced magmatic activity. However, it is obviously more intense than in the low-relief areas, as indicated by the structure of their axial zone (typical spreading cells) and the identification of high-Ca and high-Fe rocks within these structures.

At the even more southerly Segment 5, the high-relief structures distributed on the flanks are of tectonic-volcanic origin. Apparently, they were originally composed of volcanics and were similar to the large neovolcanic rise at Segment 7. Beyond the axial zone, however, they were uplifted, resulting in the exhumation of gabbroids along with volcanics on the seafloor.

The volcanics distributed in the anomalous high-relief segments are also anomalous in terms of composition and they are predominant on volcanic structures, while they are less abundant on tectonic structures compared to the depleted basalts.

Based on the isotopic-petrogeochemical study of basalts and dolerites, two types (passive and active) of chemical inhomogeneities are distinguished in the upper mantle at the level of the melting zone. From our point of view, the involvement these inhomogeneites in the process of basaltic melting led to local increases in the crustal thickness, relief growth, and the appearance of spreading cells orthogonal to the spreading axis.

Passive inhomogeneities are blocks of matter similar in composition to the mantle source EM-2, which, as we assumed, are composed of continental lithosphere rocks.

We assume that contamination of the convecting depleted oceanic mantle by these blocks occurred on the southern wing of the Charlie Gibbs FZ during tectonic erosion of the continental lithosphere under the influence of the oceanic asthenosphere during the period when the former was still present on the opposite wing of this fault.

These blocks are heterogeneous in composition and are located at different depth levels, descending to an intermediate zone between the garnet and spinel depth facies levels. Being involved in the process of melting, low-Al E-MORB volcanics occur at a deeper level, while high-Ti high-Fe N-MORB basalts are at a shallower depth level.

The deeper melts not only reached the surface but also, possibly together with fluids, contributed to metasomatic alteration of the depleted mantle forming schliers and veins. Subsequent melting of the metasomatically depleted mantle produced N-MORB basalts irregularly enriched in various lithophilic elements: Rb, Sr, Th, U, Zr, and Pb.

The melting of mantle inhomogeneities along with the depleted mantle led to an increase in the volume of melt and, accordingly, to an increase in the subaxial upwelling (diapirism) of the asthenospheric mantle. The latter resulted in a decrease in the strength of the lithosphere, intensification of magmatism in these areas, and the formation of higher relief and spreading cells orthogonal to the spreading axis.

A microplume of hotter and enriched mantle, localized under the MAR axial part in the area of a large neovolcanic rise at Segment 7, composed of oceanic tholeites T-MORB, serves as the active inhomogeneity. According to the character of distribution of Bouguer anomalies, this section has the thickest crust in the study area and/or the highest temperature of the upper mantle. It is possible that the microplume moved to Segment 7 from Segment 5 ~2.58 Ma ago, where the large Faraday Seamount was formed.

The microplume substance in the study area contains a predominant component similar to the HIMU in composition. The microplume also contains the depleted mantle matter (DM) and, to a small extent, the EM-2 component, which, judging by the higher Rb, Pb, K_2O, and P_2O_5 contents in some basalt samples of the neovolcanic uplift, contaminates the microplume unevenly.

Ascending through the depleted mantle, the microplume assimilates it and, simultaneously, the matter of the continental lithosphere blocks present in the study area.

After reaching a certain depth level, the microplume spread out. Considering that $(Sm/Yb)_n$ ratios (1.01–1.37) in T-MORB basalts are only slightly higher than that in depleted basalts, we can expect that spreading occurred at the level of spinel facies depth. The most intense flows of microplume material were formed in the subaxial spreading zone, where the strength of the surrounding mantle is the lowest due to its higher temperatures compared to those in the flank parts of the MAR.

We are able to evaluate the features of only the northern branch of this flow, which moved following the general northwestward strike of the MAR in this segment. The areas south of Segment 7 have not yet been studied. As the flow of microplume material moved, it is partially melted. The resulting melts mixed with those generated in the depleted mantle that resulted in the formation of Nb-, Rb-, and Ba-rich N-MORB tholeites.

Melting led to a decrease in the volume of flow and depletion in hygromagmatophilic and enrichment in refractory elements. To the greatest extent, the flow is expected to be cooled and depleted in lithophilic components at the Charlie Gibbs FZ. In addition, it is affected by the cooling influence of the fracture zone, which, in particular, is indicated by the near-fault occurrence of high-Na and high-Ti basalts.

However, the data on the Bouguer anomalies and the topography of the axial and crestal zones indicate greater intensity of magmatism and crustal thickness in this area. This contradiction can be avoided by assuming that the fracture zone, on the opposite wing of which is located colder and thicker lithosphere, prevents the further penetration of the flow moving from the south.

As a result, there is an accumulation of matter here and an increase in the intensity of magmatic accretion, resulting in the formation of increased axial and crestal relief, an unusual structure of the rift-transform intersection, and, judging from the distribution of Bouguer anomalies, to increased crustal thickness.

This matter preserved some of its original markers, in the form of slightly elevated K_2O, P_2O_5, Nb, and La contents in the depleted basalts of the segment adjacent to the Charlie Gibbs FZ. In addition, single samples of T-MORB tholeites were dredged here.

In the areas where the flow crossed blocks of continental lithosphere or passed over them, generated melts were also mixed with melts generated during melting of the material of these blocks. The T-MORB volcanics formed in this way contain a larger amount

of the mantle component EM-2 in their composition compared to the T-MORB basalts dredged from the volcanic rises of Segment 7. They are also distinguished by higher Th, Pb, Ba, and Sr contents. The N-MORB volcanics distributed in these areas are also selectively enriched with some of these elements and Zr as well.

There are two other types of chemical inhomogeneities in the upper mantle of the studied MAR segment.

• The first type: the almost ubiquitous enrichment of the depleted mantle in Zr and the northern part of the studied segment (from the Charlie Gibbs FZ to 49° N) also in Pb and P_2O_5. Taking into account the fact that the trends of variations of Zr and Pb contents in the depleted basalts from these regions are extrapolated to the E-MORB basalt field, one can assume that, at one of the evolutionary stages of the composition of the asthenospheric mantle, it was enriched in these elements as a result of extensive metasomatism under the influence of melts derived from the substance of continental lithosphere blocks.

• The second type is local areas of the depleted mantle enriched in Cr and Ni, which occur throughout the studied area. One of the possible explanations for this phenomenon is that the material of the depleted mantle, which had already experienced melting, participated in the melting process at these sites.

The strike of the studied MAR segment differs sharply from those both north of the Charlie Gibbs FZ and south of the Faraday polygon area. From the Azores Rise to the north, the MAR strikes in a northeasterly direction, which is probably set by flows of plume material coming from the Azores plume in a northeasterly direction [44, 56].

In this case, one can expect that the change in the strike of the MAR near the southern end of the Faraday polygon area could be related to the wedging of this flow. The question arises, however, as to why the more northern segment of the MAR has not submeridional strike, which would be more expected, since this direction is orthogonal to the spreading axis and closer to the Charlie Gibbs FZ, but the northwestward one. Furthermore, it is not only the ridge that has this strike but also numerous rift and crestal structures, which occur predominantly in low-relief areas.

Obviously, the formation of NW-striking rift structures was predetermined by the presence of the NW-striking lithosphere zones of the lowest strength, which may be more heated areas of the lithosphere. As was stated above, the latter appear in areas with higher magmatic intensity (high-relief areas) where mantle inhomogeneities with the EM-2 source material take part in melting. The latter promotes nucleation and rise of larger diapirs of asthenospheric mantle, which become centers of magmatic activity.

Moving from the south, each successive site of greater magmatic intensity (high-relief area) is displaced to the west relative to the previous one. Due to this, they are all on the same NW-striking line. The diapirs warm the lithosphere both above and adjacent to them. There appears a zone of less resistant NW-striking lithosphere between the diapirs, along which a system of echeloned breakaway cracks and basins develops during spreading.

The breakaway cracks contribute to decompression melting of the sublithospheric mantle in the areas between the diapirs, which leads to the formation of small neovolcanic ridges.

Thus, the studies have revealed that the Icelandic (to the north) and Azores (to the south) plumes have no influence on axial crustal accretion in the studied segment of the MAR. The signs of influence of the Azores plume on the MAR segment located immediately south of the Charlie Gibbs FZ mentioned above are possibly caused by other reasons. Among them are the rise of a microplume of enriched mantle, similar to the HIMU, in the segment of 48.41°–48.46° N and its subaxial spreading in the northern direction as well as the presence of blocks of the matter close to EM-2 in the composition, apparently composed of continental lithosphere rocks in the upper mantle, at the level of the melting zone.

CONCLUSIONS

(1) Areas of higher and lower magmatic productivity alternate along the MAR axis between the Maxwell and Charlie Gibbs FZs. They correspond to higher and lower bottom topography of the axial and crestal zones. Furthermore, the average elevation of both zones decreases to the north beginning from the large neovolcanic rise in the southern part of the study area and, then, increases again near the Charlie Gibbs FZ. Spreading cells oriented orthogonally to the spreading axis are formed in high-relief areas in the axial zone.

The structure of the crestal zones is dominated by uplifts of different origin: from tectonic to volcanic. The low-relief areas have a northwest strike oblique to the spreading axis. Here the rift valley consists of separate deep rift basins separated by small neovolcanic ridges; NW-striking ridges separated by wide depressions are developed on the flanks.

(2) The diversity of compositions of the studied volcanics is determined by the following processes and factors: fractional crystallization of melts during their ascent to the surface; accumulation of phenocrysts in melts; conditions of melting of primary melts: temperature, depth, degree of partial melting, heterogeneity of the melting substrate composition.

(3) Among the basalts and dolerites dredged in the study area, several petrochemical groups are distinguished:

(i) main group, which unites rocks with moderate contents of rock-forming oxides;

(ii) groups of high-Ca, high-Na, high-Ti, high-Fe, high-Ti high-Fe, high-Al volcanics, which have higher

CaO, Na_2O, TiO_2, Fe_2O_3, simultaneously TiO_2 and Fe_2O_3, Al_2O3, respectively, at the same MgO values;

(iii) a group of low-Al rocks with lower Al_2O_3 and CaO contents at higher TiO_2 and Fe_2O_3 contents.

(4) With the exception of high-Al volcanics, in which a large number of plagioclase phenocrysts led to high Al_2O_3 concentration, the appearance of other groups of basalts and dolerites is associated with differences in the melting conditions of primary basaltic melts and in the composition of the mantle substrate. The most common volcanics of the main group were formed under the most common conditions of melting characteristic of this MAR segment, which took place under moderate temperature, pressure, and degree of partial melting.

The rocks of the high-Ca group were formed of high-temperature melts and a high degree of partial melting. They are found in the centers of the most intense magmatic activity above the upwelling asthenospheric mantle in the central parts of spreading cells and on volcanic rises. Along with the high-Ca rocks, high-Fe basalts, which represent deeper melts, are common.

The rocks of the high-Na and high-Ti groups crystallized from melts generated at lower temperatures and a lower degree of partial melting. They are present near the Charlie Gibbs FZ and in areas of low-relief topography with widespread development of deep rift basin where such conditions of melting can occur.

Low-Al basalts and dolerites are predominantly distributed on the rises of the crestal zone of high-relief MAR segments. They were derived from deeper melts generated in a layer intermediate between spinel and garnet facies of depth, from a substrate enriched in lithophilic elements and radiogenic Sr, Nd, and Pb isotopes.

High-Ti high-Fe basalts, spatially associated with low-Al volcanics, were derived from the substrate of similar composition but at the level of the spinel depth facies.

(5) Oceanic tholeiites of N-MORB, T-MORB, and E-MORB types are distinguished in the studied volcanics. Oceanic N-MORB tholeiites are widespread. They were derived predominantly from the depleted mantle (DM source). E-MORB basalts and dolerites, petrochemically classified as low-Al rocks, are common in high-relief areas. Their mantle substrate is formed by a mixture of DM and EM-2 material with a subordinate role of HIMU.

T-MORB volcanics are mainly localized on large volcanic rises in the southern part of the studied MAR area. They were melted from the substrate formed by a mixture of DM and HIMU material with the subordinate role of EM-2. A small number of this type of samples are found in association with E-MORB volcanics. T-MORB volcanics are characterized by the increase in the proportion of EM-2 material, which is expressed in higher Sr, Ba, Th, and Pb contents. N and T-MORB volcanics form a series of rocks formed by mixing of their melts.

(6) There is no influence of the Azores plume on the processes of axial crustal accretion between the Charlie Gibbs and Maxwell FZs. The proposed signs of this influence are caused by the mantle inhomogeneity in this area. Two types of mantle heterogeneities are reconstructed that participate in melting: passive and active.

Passive heterogeneities are represented by blocks of continental lithosphere close to the mantle source EM-2 in composition, located at different depth levels, extended areas of metasomatically altered depleted mantle enriched with Zr or Zr, P_2O_5, and Pb, as well as blocks of possibly previously melted depleted mantle enriched in Cr and Ni.

Active inhomogeneities are associated with the uplift of the microplume of the enriched mantle close to the mantle source HIMU in composition and with its subaxial flow in the northern direction up to the Charlie Gibbs FZ. During the movement of microplume material, its partial melting occurred that resulted in its depletion in lithophilic and enrichment in refractory elements. The resulting melts mixed with those generated in the depleted mantle and in the mantle with passive inhomogeneities.

SUPPLEMENTARY INFORMATION

The online version contains supplementary material available at https://doi.org/10.1134/S0016852123050084.

ACKNOWLEDGMENTS

We are grateful to reviewers A.N. Didenko (Kosygin Institute of Tectonics and Geophysics, Far Eastern Branch of Russian Academy of Sciences, Khabarovsk, Russia) and E.P. Dubinin (Earth Science Museum at Moscow State University (Museum of Natural History), Moscow, Russia) for helpful comments and editor M.N. Shoupletsova (Moscow, Russia) for thorough editing.

FUNDING

This work was supported by the Russian Science Foundation (project no. 22-27-00036).

CONFLICT OF INTEREST

The authors of this work declare that they have no conflicts of interest.

REFERENCES

1. E. P. Dubinin, Yu. I. Galushkin, and A. A. Sveshnikov, "The model of oceanic crust accretion and its geodynamic consequences," in *Zhizn' Zemli*, Ed. by V. A. Sa-

dovnichii and A. V. Smurov (Mosk. Gos. Univ., Moscow, 2010, Vol. 32), pp. 53–83 [in Russian].

2. L. N. Kogarko, "Alkaline magmatism and enriched mantle reservoirs: Mechanisms, time, and depth of formation," Geochem. Int. **44**, 3–10 (2006).
3. A. A. Peyve, "Structural-compositional heterogeneities, magmatism and geodynamic features of the Atlantic ocean," in *Transactions of Geological Institute of Russian Academy of Sciences.* Vol. 548 (Nauchn. Mir, Moscow, 2002).
4. A. A. Peyve, S. Yu. Sokolov, A. N. Ivanenko, et al., "Accretion of the oceanic crust in the Mid-Atlantic. Ridge (48°–51.5° N) during "dry" spreading," Dokl. Earth Sci. **507**, S349–S356 (2022)
5. A. A. Peive, S. Yu. Sokolov, A. A. Razumovsky, et al., "The relationship between magmatic and tectonic processes in the formation of the oceanic crust to the south of the Charlie Gibbs Fracture Zone (North Atlantic)," Geotectonics **57** (), 42–65 (2023).
6. S. G. Skolotnev, "The nature of the diversity of volcanics in the equatorial part of the Mid-Atlantic Ridge," Prostranstvo Vremya **4** (1), 6–42 (2013). http://e-almanac.space-time.ru/assets/files/Tom
7. S. G. Skolotnev, Doctoral Dissertation in Geology and Mineralogy (Geol. Inst. Ross. Akad. Nauk, Moscow, 2015) [in Russian].
8. S. G. Skolotnev, "Different-scale segmentation of slow-spreading mid-oceanic ridges and its possible causes (on the example of the Central and South Atlantic)," in *Proceedings of L Tectonic Conference "Problems of Tectonics and Geodynamics of the Earth Crust and Mantle,"* Vol. 2 (GEOS, Moscow, 2018), pp. 189–193.
9. S. G. Skolotnev, K. O. Dobrolyubova, A. A. Peyve, et al., "Structure of spreading segments of the Mid-Atlantic Ridge between the Arkhangelsky and Bogdanov transform faults, Equatorial Atlantic," Geotectonics **56** (1), 1–20 (2022).
10. S. G. Skolotnev, A. Sanfilippo, A. A. Peyve, et al., "Geological and geophysical studies of the Charlie Gibbs Fracture Zone (North Atlantic)," Dokl. Earth Sci. **497** (1), 191–194 (2021).
11. N. M. Sushchevskaya, E. Bonatti, A. A. Peyve, et al., "Heterogeneity of rift magmatism in the Equatorial Province of the Mid-Atlantic Ridge (15° N to 3° S)," Geochem. Int. **40** (1), 26–50 (2002).
12. N. M. Sushchevskaya, G. L. Leichenkov, B. V. Belyatskii, and A. V. Zhilkina, "Evolution of the Karoo-Maud Plumeand formation of Mesozoic igneous provinces in Antarctica," Geochem. Int. **60** (6), 509–529 (2022).
13. C. J. Allegre, J.-P. Poirier, E. Humler, and A. W. Hofmann, "The chemical composition of the Earth," J. High Resolut. Chromatogr. Chromatogr. Commun., **134**, 515–544 (1995).
14. J. C. Alt, T. F. Anderson, L. Bonnell, and K. Muehlenbachs, "Mineralogy, chemistry, and stable isotopic compositions of hydrothermally altered sheeted dikes: ODP Hole 504B, Leg 111," Proc. Ocean Drill. Program: Sci. Results **111**, 27–40 (1989).
15. D. L. Anderson and K. A. Schramm, "Global hotspot maps," in *Plates, Plumes, and Paradigms*, Ed. by G. R. Foulder, J. H. Natland, D. C. Prensall, and D. L. Anderson (GSA. Spec. Pap. 2005, Vol. 388), pp. 19–29.
16. B. Benediktsdyttir, R. Hey, F. Martinez, et al., "A new kinematic model of the Mid-Atlantic Ridge between 55°55′ N and the Bight Transform Fault for the past 6 Ma," J. Geophys. Res.: Solid Earth **121** (2), 455–468 (2016).
17. Crane K. The spacing of rift axis highs: Dependence upon diapiric processes in the underlying asthenosphere? EPSL **72**, 405–414 (1985).
18. R. M. Ellam, "Lithospheric thickness as a control on basalt geochemistry," Geology **20**, 153–156 (1992).
19. J. Escartin, D. K. Smith, J. Cann, et al., "Central role of detachment faults in accretion of slow-spread oceanic lithosphere," Nature **455**, 790–794 (2008).
20. D. Fontignie and J. G. Schilling, "Mantle heterogeneities beneath the South Atlantic: A Nd–Sr–Pb isotope study along the Mid-Atlantic Ridge (3° S–46° S)," EPSL **142**, 109–121 (1996).
21. GEBCO 30″ Bathymetry Grid. Vers. 20141103. 2014. http://www.gebco.net (Accessed June, 2023).
22. GEOROC Database (Geochemistry of Rocks of the Oceans and Continents). Vers. 2023-06-01. 2023. https://georoc.eu/georoc/ (Accessed June, 2023).
23. N. R. Grindlay, P. J. Fox, and P. R. Vogt, "Morphology and tectonics of the Mid-Atlantic Ridge (25° S–27° 30′ S) from sea beam and magnetic data," J. Geophys. Res. **97** (B5), 6983–7010 (1992).
24. B. B. Hanan, R. H. Kingsley, and J. G. Schilling, "Pb isotope evidence in the South Atlantic for migrating ridge interactions," Nature **322**, 137–144 (1986).
25. S. R. Hart, "Heterogeneous mantle domains: Signatures, genesis and mixing chronologies," EPSL **90** (3), 273–296 (1988).
26. R. Hey, F. Martinez, and A. Höskuldsson, et al., "Multibeam investigation of the active North Atlantic plate boundary reorganization tip," EPSL **435**, 115–123 (2016).
27. A. W. Hoffman, "Chemical differentiation of the Earth: The relationships between mantle, continental crust, and oceanic crust," EPSL **90**, 297–314 (1991).
28. A. F. Hofman, "Mantle geochemistry: Message from oceanic volcanism," Nature **385**, 219–229 (1997).
29. E. R. Humphreys and Y. Niu, "On the composition of ocean island basalts (OIB): the effect of lithospheric thickness variation and mantle metasomatism," Lithos **112**, 118–136 (2009).
30. M. G. Jackson, S. R. Hart, and A. A. Koppers, et al., "The return of subducted continental crust in Samoan lavas," Nature **448**, 684–687 (2007).
31. A. L. Jaques and D. H. Green, "Anhydrous melting of peridotite at 0–15 kb pressure and the genesis of tholeiite basalts," Contrib. Mineral. Petrol. **73** (3), 287–310 (1980).
32. E. M. Klein and Ch. H. Langmuir, "Global correlations of ocean ridge basalt chemistry with axial depth and crustal thickness," J. Geophys. Res. **92** (B8), 8089–8115 (1987).
33. Ch. H. Langmuir and J. F. Bender, "The geochemistry of oceanic basalts in the vicinity of transform faults:

Observations and implications," EPSL **69**, 107–127 (1984).

34. Ch. H. Langmuir, J. F. Bender, A. E. Bence, et al., "Petrogenesis of basalts from the FAMOUS area: Mid-Atlantic Ridge," EPSL **36**, 133–156 (1977).
35. K. C. Macdonald, P. J. Fox, and P. R. Vogt, "A new view of the mid-ocean ridge from the behavior of ridge axis discontinuities," Nature **335**, 217–225 (1988).
36. F. Martinez, R. Hey, and A. Hoskuldsson, "Reykjanes Ridge evolution: Effects of plate kinematics, small-scale upper mantle convection and a regional mantle gradient," Earth-Sci. Rev **206**, 1–24 (2020).
37. S. Merkouriev and C. DeMets, "A high-resolution model for Eurasia–North America plate kinematics since 20 Ma," Geophys. J. Int. **173**, 1064–1083 (2008).
38. R. Montelli, G. Notel, F. A. Dahlen, et al., "Catalogue of deep mantle plumes: New results from finite-frequency tomography," Geochem. Geophys. Geosyst. **7** (11), 1–69 (2006).
39. Y. Niu and M. J. O'Hara, "MORB-mantle hosts the missing Eu (Sr, Nb, Ta and Ti) in the continental crust: new perspective on crustal growth, crust-mantle differentiation and chemical structure of oceanic upper mantle," Lithos **112**, 1–17 (2009).
40. O. Okina, S. Lyapunov, M. Avdosyeva, et al., "An investigation of the reliability of HF acid mixtures in the bomb digestion of silicate rocks for the determination of trace elements by ICP-MS," Geostand. Geoanal. Res. **40**, 583–597 (2016).
41. O. I. Okina, S. M. Lyapunov, and A. S. Dubensky, "Influence of sample treatment after bomb digestion on determination of trace elements in rock samples by ICP-MS," Microchem. J. **140**, 123–128 (2018).
42. M.G. Phillips, E. M. Parmentier, and J. Lin, "Mechanisms for the origin of mid-ocean ridge axial topography: Implications for the thermal and mechanical structure of accreting plate boundaries," J. Geophys. Res. **92**, 12823–12836 (1987).
43. M. Regelous, Ya. Niu, W. Abouchami, et al., "Shallow origin for South Atlantic Dupal Anomaly from lower continental crust: Geochemical evidence from the Mid-Atlantic Ridge at 26° S," Lithos **112**, 57–72 (2009).
44. J. Schilling, Geochemical and isotopic variation along the Mid-Atlantic Ridge axis from 79° N to 0° N, in *The Geology of North America*: *The Western Atlantic Region*, Ed. by P. R. Vogt and B. E. Tucholke (GSA Mem., Boulder, USA, 1986), pp. 137–153.
45. J. Schilling, B. Hanan, and B. McCulli, et al., "Influence of the Sierra Leone mantle plume on the equatorial Mid-Atlantic Ridge: A Nd–Sr–Pb isotopic study," J. Geophys. Res. **99** (B6), 12005–12028 (1994).
46. J. G. Schilling, G. Thompson, and R. Kingsley, et al., "Hotspot-migrating ridge interaction in the South Atlantic," Nature **313**, 187–191 (1985).
47. J. G. Schilling, M. Zajac, and R. Evants, et al., "Petrologic and geochemical variations along the Mid-Atlantic Ridge from 29° N to 73° N," Am. J. Sci. **283**, 510–586 (1983).
48. S. G. Skolotnev, A. Sanfilippo, and A. A. Peyve, et al., "Seafloor spreading and tectonics at the Charlie Gibbs transform system (52°–53° N, Mid-Atlantic Ridge): Preliminary results from R/V "Akademik Nikolaj Strakhov" expedition S50," Ofioliti **46** (1), 83–101 (2021).
49. N. H. Sleep, "Tapping of magmas from ubiquitous mantle heterogeneities: An alternative to mantle plumes?" J. Geophys. Res. **89** (B12), 10029–10041 (1984).
50. A. V. Sobolev, A. W. Hofmann, D. V. Kuzmin, et al., "The amount of recycled mantle-derived melts," Science **316**, 412–417 (2007).
51. S. S. Sun and W. F. McDonough, "Chemical and isotopic systematics in ocean basalt: Imlication for mantle composition and processes," in *Magmatism in the Ocean Basins*, Ed. A. D. Saunders, M. J. Norry (Spec. Publ.—Geol. Soc. USA, 1989, Vol. 42), pp. 313–345.
52. S. S. Sun, R. W. Nesbit, and A. Ya. Sharaskin, "Geochemical characteristics of mid-ocean ridge basalts," EPSL **96**, 119–133 (1979).
53. R. N. Thompson, "Phase-equilibria constraints on the genesis and magmatic evolution of oceanic basalts," Earth-Sci. Rev. **24**, 161–210 (1987).
54. B. L. Weaver, D. A. Wood, J. Tarney, et al., "Geochemistry of ocean island basalts from the South Atlantic: Ascension, Bouvet, St. Helena, Gough and Tristan da Cunha," Spec. Publ.—Geol. Soc. London, No. 30, 253–267 (1987).
55. W. M. White, "Ocean island basalts and mantle plumes: The geochemical perspective," Ann. Rev. Earth Planet. Sci. **38**, 133–160 (2010).
56. W. White and J. G. Schilling, "The nature and origin of geochemical variation in the Mid-Atlantic Ridge basalts from the central North Atlantic," Geochim. Cosmochim. Acta **42**, 1501–1516 (1978).
57. R. B. Whitmarsh, A. Ginzburg, and R. C. Searle, "The structure and origin of the Azores-Biscay Rise, Northeast Atlantic Ocean," J. Geophys. Res. **70**, 79–107 (1982).
58. D. Yu, D. Fontignie, and J. G. Schilling, "Mantle-plume interactions in the Central North Atlantic: Nd-isotope study of Mid-Atlantic Ridge basalts from 30° N to 50° N," EPSL **146**, 259–272 (1997).
59. A. Zindler, E. Jagoutz, and S. Goldstein, "Nd, Sr and Pb isotopic systematics in a three-component mantle: A new perspective," Nature **298**, 519–523 (1982).

Translated by D. Voroshchuk